Applied Thermal Engineering 218 (2023) 119296

Contents lists available at ScienceDirect

Applied Thermal Engineering

journal homepage: www.elsevier.com/locate/apthermeng

Research Paper

Study of recirculating water-based and carbon-based working fluids on the combustion flow field and the cycle performances of semi-closed CO_2-capturing Brayton-derived cycles

José Francisco González Álvarez [a,*], Ahmad K. Sleiti [b], Wahib A. Al-Ammari [b], Efrén Alonso Fernández [c]

[a] Universidad de León, Spain
[b] Department of Mechanical & Industrial Engineering, College of Engineering, Qatar University, Doha 2713, Qatar
[c] Drotium

ARTICLE INFO

Keywords:
Semi-closed Brayton cycle
Water cycle
CO_2 capture
Oxy-combustion
Performance analysis
Combustion CFD analysis

ABSTRACT

The transition into new power technologies that utilize fossil fuels with near zero emissions to the ambient is an urgent need to mitigate the worldwide environmental problems. In this study, detailed analyses of carbon-based and water-based oxy-combustion power cycles are introduced. The applied methodologies to perform these analyses comprise CFD analysis of reacting flows for dual recuperative cycle (DRC) and reheated cycle (RHC). The employed CFD methodologies used the non-simplified Navier-Stokes formulation of reacting flows to avoid the use of extra models or assumptions. It was found that recycling carbon-based fluids would allow better overall performances of the resulting cycles. Recycling water-based fluids, however, would provide some interesting features regarding the temperature field in the combustion chamber. Hence, it would avoid in a better way the possibility of facing overheating caused by oxy-combustion, as well as provide some valuable aerodynamic features for the turbines. When analyzing the obtained combustion flow field, CO_2 and H_2O working fluids create a more important temperature abatement in the flame surrounding areas and trail than Air. When comparing CO_2 and H_2O working fluids between them, the H_2O working fluid initially showed a slightly bigger high-temperature zone than the CO_2 working fluid. Despite this fact, and after those initial zones, the H_2O working fluid showed a more important temperature abatement than the CO_2 working fluid, except for the transversal tip of the flame trail, where temperatures are in a safe range for superalloys. When considering the temperature on the fluid domain symmetry axis and at the outlet, for the 30 atm case (30.4 bar), it was found that the CO_2 fluid presented a temperature equal to 86.9% of the Air one in the same location and pressure, whereas the H_2O fluid presented an 82% of the Air one. In addition, thermoeconomic analyses were conducted for the DRC and RHC that are working at high pressure of less than 42 bar and operating temperatures of 1100 K to 1450 K to ensure feasible design for the cycle components. Furthermore, it is found that a maximum efficiency of 47.50% is obtained by the carbon-based RHC under wet-cooling conditions and a minimum cycle efficiency of 33.54% is obtained by the water-based DRC under dry-cooling conditions. From an economic point of view, the average LCOE of the present carbon-based and water-based cycles is 4.17 ¢/kWh, which is 28% lower than the average LCOE of the supercritical carbon-based and integrated gas-turbine-based cycles. Moreover, the LCOE of the carbon-based RHC is minimum (3.92 ¢/kWh) at minimum cycle temperature (T_{min}) of 305 K (wet cooling) and identical to the water-based RHC (4.00 ¢/kWh) at T_{min} of 323 K (dry-cooling).

1. Introduction

The increase of the worldwide energy demand driven by rapid economic and population growth aggravates the global environmental problems including greenhouse gas emissions and the depletion of the ozone layer. This is mainly caused by the combustion of fossil fuels to meet the energy demand rather than the transition and utilization of clean energy resources [1]. The Kyoto Protocol [2], the Paris Agreement [3], COP26 Climate Pact [4] or the directive 2018/410 of the European

* Corresponding author.
E-mail address: josefrancisco.g.a@gmail.com (J.F. González Álvarez).

https://doi.org/10.1016/j.applthermaleng.2022.119296
Received 6 June 2022; Received in revised form 14 August 2022; Accepted 6 September 2022
Available online 17 September 2022

Nomenclature

ASU	Air Separation Unit
C_ξ	volume fraction constant
C_τ	time scale constant
DRC	dual recuperative cycle
D_{ij}	diffusion coefficients
$D_{T,i}$	thermal diffusion coefficient of the ith species
h	enthalpy
$\overrightarrow{j}_i$	diffusion flux of the ith species
$\overrightarrow{j_i^d}$	diffusion part due to gradients in species concentrations
$\overrightarrow{j_i^p}$	diffusion part due to the pressure difference
$\overrightarrow{j_i^T}$	diffusion part due to differences in temperature
$\overrightarrow{j_q}$	heat flux density
$\overrightarrow{j_q^c}$	heat flux due to conduction
$\overrightarrow{j_q^d}$	heat flux due to diffusion
$\overrightarrow{j_q^D}$	heat flux due to Dufour effect
k	turbulence kinetic energy
LCOE	levelized cost of electricity
M_i	molar mass of the ith species
ORC	organic Rankine cycle
PR	pressure ratio
P_{max}	maximum cycle pressure
P_{min}	minimum cycle pressure
p	pressure
$\overline{\overline{p}}$	momentum change due to viscous dissipation and pressure
q_r	heat generation due to radiation
RHC	reheating cycle
r/d	nondimensionalized radial position
t	time
T_{max}	maximum cycle temperature
T_{min}	minimum cycle temperature
T	temperature
$\overrightarrow{V}$	velocity
x/d	nondimensionalized axial position
Y_j	mass fraction of the species j
ε	turbulent dissipation rate
λ	mixture's thermal conductivity
ν	kinematic viscosity
ξ^*	length fraction of the fine scales
ρ	density of a mixture
ρ_i	density of the ith species
σ	Stefan-Boltzmann constant
$\sum$	flame area density
$\overline{\overline{\tau}}$	stress tensor
τ^*	reaction time in the fine scales
ω_i	molar rate of formation of the ith species

Union are examples of substantial international interest in reducing greenhouse gas emissions. According to different organizations such as the European Environment Agency [5] and the United States Environmental Protection Agency [6], the present level of such emissions is an international concern.

Among several efforts and innovations that were made and proposed to reduce greenhouse gas emissions, the utilization of renewable energy resources is considered one of the most feasible solutions to obtain this goal [7]. However, the intermittency nature of renewable energies limits their commercial applications as their energy costs are relatively higher than fossil-fuel-based energy [8]. The high cost of renewable-based energy is mainly owned to the high cost of energy storage equipment such as thermal energy storage in concentrated power plants, and batteries used with solar photovoltaic energy. As fossil fuels are considered to be the major source of global energy, at least in the middle term [8], it is necessary to implement advanced power generation technologies that efficiently utilize fossil fuels with near zero emissions to the ambient. This could be achieved by collecting these gases and avoiding their release into the atmosphere [9] using one of three capturing technologies including a) post-combustion capture, b) pre-combustion capture, and c) oxy-combustion capture.

In post-combustion technology, CO_2 is removed from the flue gas after the execution of the combustion process. This capture can be performed using absorption technologies employing amine-based products such as monoethanolamine (MEA) [10] (some other amine-based products can also be used for this purpose [11]). The use of new advanced solvents is studied as well [12]. Other possible technologies would be adsorption, physical separation (for example using membranes), and phase change performing partial liquefaction. Important advances have also been achieved in the field of porous ionic liquid-derived materials [13] as well as in novel poly(ionic liquid)-based aerogels [14] applied to CO_2 capture. Although this technology is proven for small-scale power plants, its large parasitic load limits its economic feasibility for large-scale systems [15]. In pre-combustion capture, CO_2 is removed after the treatment of the fuel before the combustion process [16]. It involves the gasification process that converts the fuel into a syngas consisting of H_2 and CO. However, this technology is limited to coal-gasification plants and suffers from high parasitic power demands. In oxy-combustion technology, combustion is performed with pure oxygen as an oxidant and recirculated fluid (CO_2 or water) as a dilution agent. One of the most significant drawbacks of this type of cycle is the need for an Air Separation Unit (ASU) continually supply the required oxygen [17]. This device has a substantial impact on the performance of the whole cycle (a 10% according to Kvamsdal et al. [18]). However, one of the most interesting points of this type of cycle is that they are built as a modification of Brayton and other gas-turbine-related cycles.

Independently of the process used to capture the carbon dioxide, mainly two complimentary options are available to complement the capturing process either by the storage of the captured CO_2 or reuse it in commercial applications. Considering the vast amounts of carbon dioxide generated in current power generation [19], geological options are the most appropriate option for the storage of the captured CO_2 [20]. Some of the chemicals which can be produced from the captured CO_2 are Methanol [21], Biodiesel (as well as other substitutes for diesel), using micro-algae for this purpose [22], Methane [23], Oxymethylene dimethyl ethers [24], and Synthesis gas [25].

Recently, oxy-combustion technology is widely investigated for power generation using highly efficient and compact supercritical [26] carbon-based power schemes. These schemes recirculate the CO_2 as the working fluid (carbon-based cycles) at supercritical conditions to harness the dense behavior of the CO_2 at these conditions. Other few studies have proposed the recirculation of the water as a working fluid instead of the CO_2 (water-based cycles). A simplified diagram of the background water cycle in which this article is developed is provided in Fig. 1, which is a modification of semi-closed Brayton cycles [26 27]. In this case, the recycled fluid is water instead of carbon dioxide.

The oxy-combustion-based cycles (mostly carbon-based cycles) were investigated from energetic, exergetic, and economic points of view at operating pressure higher than 200 bar and temperatures from 550 °C to 1150 °C [18 28]. But the commercial development of the cycle

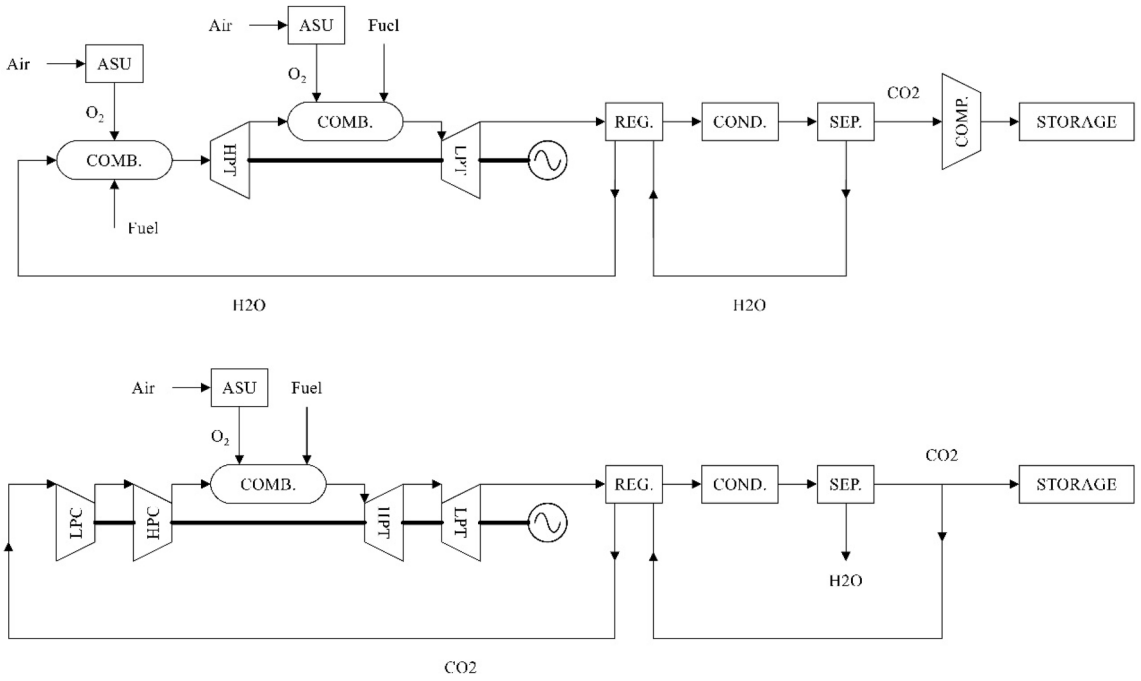

Fig. 1. Schematic background H_2O cycle (top) and semi-closed Brayton cycle (bottom). 'COMB.' represents a combustion chamber; 'ASU' an Air Separation Unit; high and low-pressure turbines (HPT, LPT); 'REG' the regenerator; 'COND.' the condenser; 'SEP.' the water separator and 'COMP' a compression stage to adapt pressure of the CO_2 exit flow to the storage pressure.

components that support these conditions is not available as these components (turbines, compressors, and heat exchangers) are still under the research and demonstration phase [29]. In contrast, the power plant components that withstand operating pressure up to 40 bar at high temperatures are already available for commercial gas power plants [30]. Thus, this study, for the first time, investigates both carbon-based and water-based oxy-combustion cycles at high pressure of 40 bar and temperature of less than 1200 °C to ensure their technical feasibility because of the mature commercial gas power plants.

A few studies were implemented on the oxy-combustion and oxygen-enriched combustion processes using CFD techniques. Prieler et al. [31] investigated the application of a steady flamelet approach on a lab-scale and an industrial furnace for different oxygen concentrations. They confirmed that the used CFD approach is capable of predicting the temperature and heat fluxes in high-temperature furnaces. Similarly, Mayr et al. [32] developed A zero/one-dimensional thermodynamic model to be used in the determination of the oxygen-enriched combustión effect on the heat transfer, gas, and wall temperatures in a high-temperature furnace. Other works have numerically studied gas turbine combustors performing oxy-combustion, focusing in that case on ammonia/kerosene fuels [33]. When comparing to the following reference by the same author [26], this work studies combustion in water and CO_2-recycling cycles, being this way water one of the cycle's working fluids instead of just a carbon-based fluid.

As techno-economic analysis is essential for the assessment and comparison of various energy systems [34 35], it is applied for the oxy-combustion system from gas-turbine-derived cycles [36 37]to oxy-fuel combustion of biomass-obtained biogases [38]. In particular, the techno-economic analysis of carbon-based cycles was investigated for various types of energy sources including coal [39], flare-gases [40], waste-heat [41], nuclear energy [42], and solar energy [43]. Recently, a thorough techno-economic performance analysis of various carbon-based cycles under design and off-design conditions is introduced by Al-Ammari and Sleiti [28].

From the aforementioned studies, it is noted that these studies mainly focused on the analysis of the water-based and carbon-based cycles from a performance point of view. This implies that the whole cycle's behavior is known, but not the detailed phenomenology within each component. Thus, in this article, one of the objectives is to gather knowledge of the detailed phenomenology when performing combustion in water- and carbon-based cycles. This article can help different authors study water and CO_2-recirculating cycles using a performance point of view.

Considering the proposed objectives in this article, the employed methodology is Computational Fluid Dynamics (CFD) for reacting flows. As a first step, the selected methodologies were validated against experimental data by the first author of this article [26]. After their accuracy has been verified, combustion in water cycles is studied and compared to combustion in other oxy-combustion cycles. Special attention is given to the conditions at the outlet of the combustion chamber. This location is essential since it is the inlet of the turbines (components dedicated to transferring power to the compressors and the electrical power generator). The effect of different operating pressures found in these cycles' combustion chambers is also studied.

Furthermore, the sensitivity analysis of the carbon-based and water-based cycles for two configurations (dual recuperative cycle and reheating cycle) is conducted for the major operating conditions from energetic and economic points of view. It is the first thermoeconomic analysis performed for these types of cycles at a high operating pressure of less than 42 bar. In addition, the thermoeconomic performance of the present cycles is compared with other cycles available in the literature.

To summarize, the main innovation points of the present study are:

- Applying CFD analysis for the combustion process in the oxy-combustion power cycles.
- Investigating the performance of carbon-based and water-based oxy-combustion power cycles at operating conditions similar to the existing gas power plants.
- Conducting thermoeconomic analysis for dual recuperative and reheated power schemes that are working with CO_2 and water as working fluids.

The rest of the manuscript is organized as follows: Section 2 presents the methodology of the CFD and thermoeconomic analyses that were

conducted in this study. Section 3 introduces the information on the conducted CFD simulations. Then, the results of the oxy-combustion CFD flow field were discussed in section 4. After that, the results of the thermoeconomic analysis were presented and discussed in Section 5. Finally, the main findings and conclusions of this study were summarized in Section 6.

2. Methodology

2.1. Computational fluid dynamics (CFD) methodology

Navier-Stokes equations provide the solution of fluid flows. When talking about reacting flows, the same group of equations can be applied to solve the problem if a more general formulation of these equations is used [44].

Without considering reactions and mixing, the Navier-Stokes equations are composed of the mass conservation equation and the momentum conservation equation. The energy conservation equation would just be needed if heat transfer is taken into account.

If reactions and mixing are considered, a more general formulation is necessary to obtain the fluid flow. In this article, this general formulation is used, which is composed of the following equations:

- One mass conservation equation per species is included in the reaction mechanism. In this article, the detailed GRI-Mech 3.0 mechanism [45] is used, which has 53 species in the 325 elementary reactions that compose it.
- Momentum and energy conservation equations
- Radiation

The use of the state equation is also necessary to close the problem. Given that the operating pressures in this article are not excessively high (they do not exceed 40 atm, 40.53 bar), the ideal gas law was used.

The use of one mass conservation equation per species could have been avoided using other simplified formulations:

- C- Equation model [46]: in this case, equations of mass conservation are replaced by a scalar reaction progress variable, 'C'. This variable describes the evolution of the reaction progress. It also needs additional models to compute the turbulent flame speed in the 'c' transport equation. The Zimont model [47] or the Peters model [44] are typically used to calculate the turbulent flame speed.
- G-Equation model [46]: this option, usually referred to as the level set approach [44], replaces the mass conservation equations with one variable. In this case, this variable is a non-reacting scalar typically called 'G'. The key point in comparison to the C-Equation model is that, in the previous case, the 'c' variable was a progress variable defined as a normalized temperature or mass fraction. In this case, however, the 'G' variable is defined as and non-reacting scalar instead. This concept was initially introduced by Markstein [48].

These two models were not used in this article because they need the laminar flame speed to compute the turbulent flame speed. This is performed typically using the Zimont model [47 49] or the Peters model [44 50]. These laminar flame speed [51] data were not currently available for the pressures studied in this article.

- Extended Coherent Flamelet Models: the formulation of these models is similar to the C-Equation model. In this case, however, the source term of the variable 'C' is more precisely modeled using an additional flame density equation '$\sum$'. These models assume that the flame thickness is smaller than the Kolmogorov scale. The effect of turbulence is taken into account considering that it wrinkles the flame front without distorting its inner structure. Hence, a more significant area would be available, allowing a higher consumption of reactants and increasing the flame velocity. These models would suit the Flamelet Regime, located in the Borghi Diagram [52] zone with a Damköhler number > 1 and a Karlovitz number less than 1. The additional equation employed to model the transport of the net flame area per unit also requires the use of closures. Some examples of these closures are the Veynante [53], the Meneveau [54], the Poinsot [54], or the Teraji [55] closure models. The solution can be significantly modified depending on the closure model employed, even without changing the oxidant or the fuel used [56]. This has been the main reason why these models have not been employed in this article.

Another alternative that could have been used to perform the target simulations in this article could have been the Probability Density Function (PDF) methods by Pope [57]. These methods have not been used since they are further costly in computational terms than the employed methodology.

2.1.1. CFD governing equations

Taking into account what has been previously exposed, the employed governing equations are shown below.

The species conservation equations are shown in Equation (1) in terms of the different species' densities.

$$\frac{\partial \rho_i}{\partial t} + div\left(\rho_i \overrightarrow{V}\right) + div\,\overrightarrow{j}_i = M_i \omega_i \tag{1}$$

The term $M_i\omega_i$ represents the production-consumption term of the i^{th} species from the chemical reaction.

Considering that the aim simulations in this article do not contain a fluid bed reactor in their setup, the production-consumption term that would model it was not considered. This term would have taken into account the addition or consumption of the i^{th} species from the disperse phase.

The term $\overrightarrow{j}_i$ represents the fluxes created by diffusion.

Ansys Fluent employs these equations written in terms of the local mass fractions. This reduces the number of required equations. If the reaction mechanism contains N species, then it would be needed N-1 equations. The N^{th} would be calculated as $Y_N = 1 - \sum_1^{N-1} Y_i$.

Considering that the detailed Grimech 3.0 reaction mechanism [45] has 53 species involved in 325 reactions, it was necessary to use 52 conservation equations.

To model the $M_i\omega_i$ terms, it was taken into account that the studied fluid flow is turbulent. The Arrhenius equations [58], which provide the exact solution for these terms in laminar flows, are not accurate in turbulent flows.

Thus, the Eddy Dissipation Concept model (EDC) by Magnussen et alia [59] was used to compute these terms. This model assumes that combustion takes place in small turbulent structures. These small turbulent structures were named 'fine scales'. In these structures, reactions take place as a constant pressure reactor over a time scale τ^*, and are governed by the Arrhenius expressions. The current temperature and species in the cells are also taken as initial conditions to perform the different integrations.

The 'fine scales' length fraction [60] can be modeled as explained in Equation (2):

$$\xi^* = C_\xi \left(\frac{\nu\varepsilon}{k^2}\right)^{1/4} \tag{2}$$

Where:

'*' represents fine-scale values.

$C_\xi = 2.1377$ represents the volume fraction constant.

ν = Kinematic viscosity.

The 'fine scales' volume fraction was modeled as ξ^{*3}.

The species in the reaction mechanism react in the 'fine scales' according to the chosen reaction mechanism during a time-scale modeled

as explained in Equation (3).

$$\tau^* = C_\tau \left(\frac{\nu}{\varepsilon}\right)^{1/2} \tag{3}$$

Where:

'*' represents fine-scale values.

$C_\tau = 0.4082$ represents the time scale constant.

The $M_i\omega_i$ terms in Equation (1) are calculated as explained in Equation (4):

$$M_i\omega_i = \frac{\rho(\xi^*)^2}{\tau^*\left[1-(\xi^*)^3\right]}\left(Y_i^* - Y_i\right) \tag{4}$$

Y_i^* are the mass fractions of the 'fine scale' τ^*.

The momentum conservation equations are given as:

$$\frac{\partial(\rho\vec{V})}{\partial t} + div\left(\rho\vec{V}\vec{V}\right) = -grad(P) + div(\bar{\bar{\tau}}) + \rho\vec{g} \tag{5}$$

The energy conservation equation [46] is shown in Equation (6). It was written in this case in terms of enthalpy.

$$\frac{\partial(\rho h)}{\partial t} - \frac{\partial p}{\partial t} + div\left(\rho\vec{V}h + \vec{j_q}\right) + \bar{\bar{p}} : grad\vec{V} - div\left(p\vec{V}\right) = q_r \tag{6}$$

The $\vec{j_q}$ term computes the density of heat flux, ':' computes a two-tensor contraction, which leads to a scalar, and q_r computes the generation of heat caused by radiation.

The $\vec{j}_i$ terms in Equation (1) can be modeled as shown in Equation (7) through Fick's Law. They are divided into three different contributions: the diffusion contribution created by species-concentration gradients (generally known as ordinary diffusion), $\vec{j_i^d}$; the diffusion contribution by temperature differences, $\vec{j_i^T}$; and the diffusion contribution by pressure differences $\vec{j_i^p}$ [46].

$$\vec{j}_i = \vec{j_i^d} + \vec{j_i^T} + \vec{j_i^p} \tag{7}$$

The term $\vec{j_i^p}$ is typically negligible in combustion reactions.

Since the employed GRI-Mech 3.0 mechanism [45] contains 53 species, a more generalized Fick's law is used to take into account multicomponent diffusion, obtained to take into account the Maxwell-Stefan equations [61].

Accordingly, diffusion is modeled as explained in Equation (8).

$$\vec{J}_i = -\sum_{j=1}^{N-1}\rho D_{ij} grad\left(Y_j\right) - D_{T,i}\frac{grad(T)}{T} \tag{8}$$

Where:

Y_j is the mass fraction of species j.

D_{ij} are the coefficients employed in the generalized Fick's law [61].

$D_{T,i}$ is the ith species coefficient of thermal diffusion.

The Fourier's Law, presented in Equation (9), was employed to model the heat fluxes $\vec{j_q}$. These fluxes are composed of three different parts: the part caused by conduction, denoted as $\vec{j_q^c}$, the part caused by the Dufour effect, denoted as $\vec{j_q^D}$, and the part caused by diffusion, denoted as $\vec{j_q^d}$.

$$\vec{j}_q = \vec{j_q^c} + \vec{j_q^D} + \vec{j_q^d} \tag{9}$$

The Dufour term, $\vec{j_q^D}$, is typically considered negligible in combustion, becoming Equation (9) as shown in Equation (10).

$$\vec{j}_q = \vec{j_q^c} + \vec{j_q^d} = -\lambda gradT + \Sigma h_i \vec{j}_i \tag{10}$$

The mixture's thermal conductivity was denoted as 'λ'. The $\vec{j}_i$ fluxes in Equation (10), caused by diffusion, were modeled, as explained in Equation (8).

The q_r term in Equation (6), energy equation, was calculated through the discrete-ordinates method. This method was employed in its conservative variant, also known as the finite-volume scheme [62]. This term should be considered in combustion, if possible, because of its decisive influence. According to the Stefan-Boltzmann law [63], it could be described as $q_{rad} = \sigma(T_{max}^4 - T_{min}^4)$. '$\sigma$' denotes the constant of Stefan-Boltzmann.

Considering that the main working point of turbomachine-derived devices is steady [64], as it is the performed test case, the simulations performed in this article are steady. Accordingly, time derivatives were neglected.

2.2. Performance analysis methodology

2.2.1. Performance analysis governing equations

Referring to Fig. 2(a), the recycled flow (state 9) is mixed and combusted with the fuel (state 10) and oxygen (state 11) in the oxy-combustor and leave at a maximum temperature of (1100 K to 1450 K). Then, the combustion products expanded in the turbine to the low-pressure side of the cycle (state 2, at a pressure of 1.5 to 5 bar) and pass through high-temperature and low-temperature recuperators (HTR (2–3), LTR (3–4)) to preheat the recycled flow before the combustion (process 7–9). Then, the combustion products are precooled in the precooler (process 4–5) to a minimum temperature of 305 K to 323 K, and the water content is removed from the CO_2 stream in the water separator (process 5–6). Then, the CO_2 is compressed to maximum pressure at state 7 (21–42 bar) at which the excess CO_2 is exported, and the recycled flow passes through the LTR and HTR to be preheated before the combustion and reaping the cycle. The energy models of each cycle were developed by applying the mass and energy conservation principles of each component, such that [65 66]:

$$\sum \dot{m}_i = \sum \dot{m}_o \tag{11}$$

$$\sum \dot{Q} + \sum \dot{m}_i h_i = \sum \dot{W} + \sum \dot{m}_o h_o \tag{12}$$

Furthermore, the thermodynamic model of the LTR, HTR, IC, and PC was based on the effectiveness method using Eq. (13) [29]: where variable specific heat of the CO_2 as a function of temperature is taken into consideration using discretized-based logarithmic mean temperature difference approach as detailed in [66].

$$\in = \frac{\dot{Q}}{\dot{Q}_{max}} \tag{13}$$

The thermal efficiency for each cycle is expressed as the ratio of the net output power ($\dot{W}_{net}$) to the total input power ($\dot{Q}_{in}$) as:

$$\eta_{th} = \frac{\dot{W}_{net}}{\dot{Q}_{in}} \tag{14}$$

where the equations of $\dot{W}_{net}$, and $\dot{Q}_{in}$ are given in the supplementary material (Table SM.1).

The economic assessment of the present cycles is presented in terms of the LCOE, [66]:

$$LCOE = \frac{PC - PV_{DTS} + PV_{LOC} - PV_{SC}}{LEP} \tag{15}$$

where the project cost (PC) is the sum of the components and installation costs (given in Eq. (16)), the depreciation tax shield present value (PV_{DTS}), and lifetime operation costs (PV_{LOC}) are expressed in Eq. (17) and Eq. (18), respectively. The present value of salvage costs (PV_{SC}) is assumed to be $0.00, while the lifetime electrical production (LEP) is given in Eq. (19).

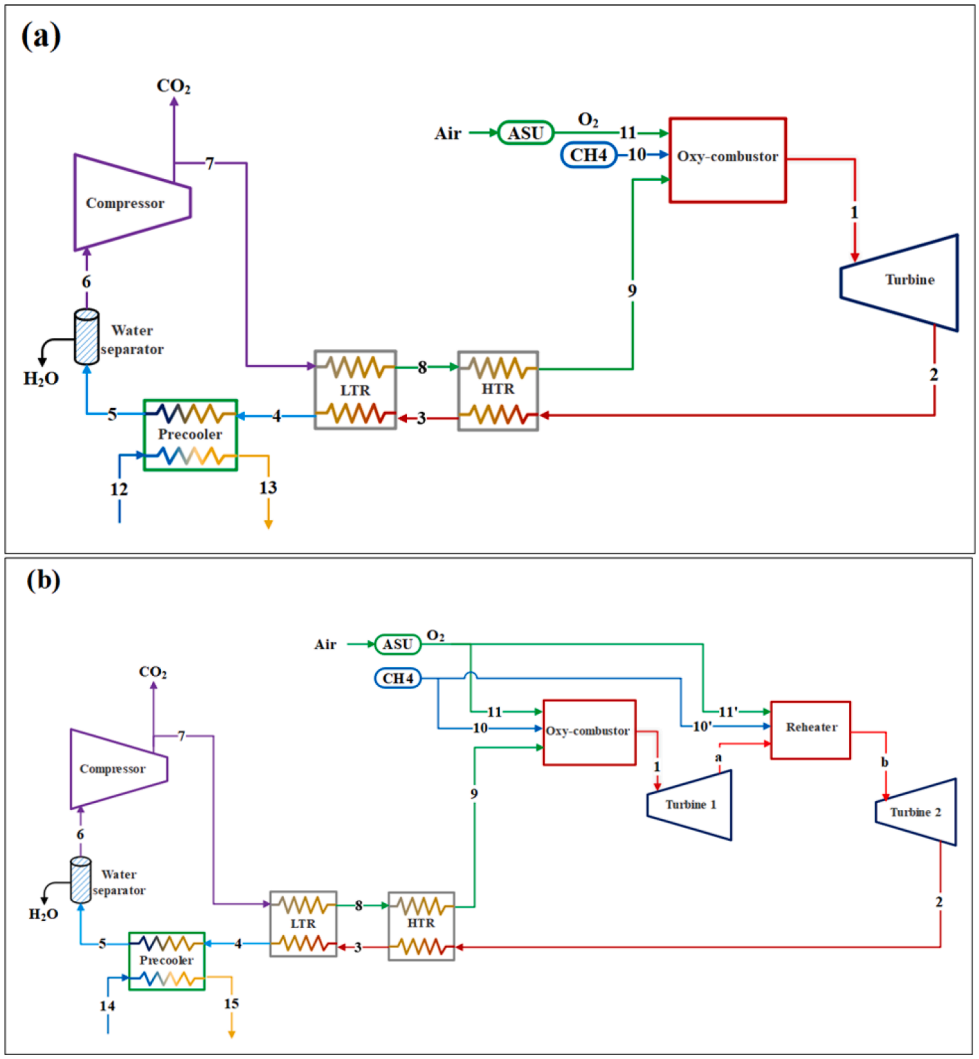

Fig. 2. Schematic diagram of carbon-based (a) Dual recuperative cycle (DRC) and (b) reheating cycle (RHC).

$$PC = \sum (Componentcost + Installationcost)_k \tag{16}$$

$$PV_{DTS} = TR \times PC/(1 + DR)^{DP} \tag{17}$$

$$PV_{LOC} = n^{*}(OMC + Costofthefuel)/(1 + DR)^{n} \tag{18}$$

$$LEP = PUF \times n \times \dot{W}_{net} \times 8760 \tag{19}$$

The design values of the parameters presented in Eqs. 16–19 are presented in [66] and [29]. Also, the capital cost functions of each component are presented in the supplementary material (Table SM.2). Furthermore, the direct labor and installation costs were taken as 12% of the capital component cost [66].

3. CFD simulations and validation

The different CFD simulations presented in this article were performed using Ansys Fluent. Further information about them is shown below.

3.1. CFD simulations validation and information

The models described in the methodology part of this article "2.1. Computational Fluid Dynamics (CFD) methodology" and section "3.4. Oxy-combustion CFD models information" were validated through reference [26] by the same author. A summary of the results found in reference [26] when validating the temperature and flow field is shown below in this section. An additional oxy-combustion temperature validation is performed in section "4.1. Temperature field results" of this article. Section "3.2. Air-fired and oxy-combustion CFD predicted deviations" also presents a further analysis of the predicted deviations between air-fired and oxy-combustion CFD simulations. Section "3.4. Oxy-combustion CFD models information" presents further detailed information about the CFD oxy-combustion simulations performed. The different CFD simulations performed in this article and reference [26] by the same author were performed using Ansys Fluent.

In article [26], a fully-premixed experimental piloted methane-air flame in stoichiometric conditions was tested and validated. This flame (called F3) [67] is located in the Distributed Reaction Zone in the Borghi diagram, more precisely at the Flamelet Regime border. The target cases studied in this article are different modifications of the case validated in reference [26].

The Navier-Stokes equations were used in their RANS (Reynolds Averaged) form. To take into account that different turbulence models may affect the obtained solutions in combustion [68], a screening of different turbulence models was performed in reference [26] for the F3 flame, which is taken as the basis of the study. In this way, the following models were checked: the Reynolds Stress Model (RSM), the standard K-Omega model, and the K-Epsilon model.

The obtained results were compared to the experimental data ob-

tained by Chen et alia [67]. The K-Epsilon model, being used with $K_{\varepsilon 2} = 1.87$ (as proposed by Jeng and Faeth [69]), was found as the model that provided better results for this case.

A reasonable agreement between the calculations and the reference data was found when comparing the obtained temperature and flow field results with the experimental data. The primary deviations in the temperature field were found near the fuel inlet, where an overheated zone was located. This fact was expected because of the use of the EDC model to calculate the production terms in the Navier-Stokes system of equations.

The EDC model is prepared to simulate turbulent flows. Since the F3 flame has a stabilizing surrounding laminar pilot flame in its setup, this secondary flame had to be modeled as a hot flow of products. This secondary flow of products was injected into the fluid domain directly at their chemical equilibrium temperature in combustion under these conditions.

Taking this into account, the presence of an overheated zone near the injector was expected. Along with that, the absence of a conventional temperature development, as it would be found in a flame, also created a slightly underheated zone far away from the injector. Since the target cases of this article do not contain pilot flames in their setup, the previously mentioned deviations are not important.

3.2. Air-fired and oxy-combustion CFD predicted deviations

The CFD methodology employed in this article consisted of non-simplified CFD formulations. In this way, the complete version of the Navier-Stokes system of equations was used rather than simplified variations. These simplified variations would have made the study cases less computationally demanded, but, at the same time, additional models or closures would have been needed. That required additional closures or models were initially developed for air-fired flames, thereby adding additional noises. An example of these possible deviations when changing different closures or models is contained in the reference [56]. In this previous reference, significant variations were found from one model to another even without changing the fuel or the oxidant.

The methodology used in this article, however, although much more demanded in computational terms than the simplified methodologies, avoids the use of additional models or closures. That was the reason why the non-simplified methodology was used in this article.

For all the simulations contained in this article, the employed reaction mechanism is the same used in reference [26]. As was previously explained, the employed reaction mechanism is the detailed GRI-Mech 3.0 [45]. This mechanism contains 53 different species in 325 elementary chemical reactions.

Regarding the suitability of the employed GRI-Mech 3.0 complete reaction mechanism when applied to oxy-combustion, reference [70] shows a reasonable agreement between the employed reaction mechanism and experimental data in the range of pressures studied in this article.

The simulated cases in this article constitute various modifications of the experimental F3 flame and are carried out using the methods explained in the methodology part of this article and verified in reference [26] by the same author. As shown in section 4.1, the employed models show a reasonable accuracy in temperature when compared to experimental oxy-combustion data. Reference [26] also showed a reasonable agreement when considering the flow field. To minimize the effect of the differences between the performed comparisons to experimental data in reference [26] and the studied cases, a general non-simplified CFD formulation was employed to avoid possible noises from additional models. Other comparison results to experimental data are shown in section 3 of this article.

3.3. Selection of the studied operating pressures

In this article, the main differences in a combustion flow-field between performing combustion surrounded by CO_2 and surrounded by H_2O are studied. These flows could be representative of semi-closed Brayton-derived cycles recirculating a carbon-based fluid in one case and a water-based fluid in the other.

The basic diagram of the water cycles is shown in Fig. 1. Considering the connection with semi-closed Brayton cycles, it is compulsory to consider the features of current gas turbines in the market. To choose what operating pressures should be studied in the combustion chambers of this type of device, two main observations are made. Firstly, cycles can be tuned searching for possible ways to improve their global efficiency and other parameters. An example of this type of analysis can be found in the following reference by Anderson et alia [71]. Secondly, if current turbomachines in the market could be reused, that would create enormous savings when using this type of cycle. Additionally, turbomachinery manufacturers would not have to redesign their existing models. Furthermore, companies dedicated to electricity production would not have to spend more money buying completely new equipment.

Considering the previous reasons, the reuse of existing equipment was taken as the most important point when selecting the operating pressures to be studied. Some specifications of different modern gas turbines are shown in Table 1. The values provided in this table are taken as references to select the operating pressures to be studied.

Three different operating pressures were taken from Table 1 to be studied. The lowest of them would be, at the same time, representative of the working pressure in the second combustion chamber of these cycles.

3.4. Oxy-combustion CFD models information

The simulations performed in this article are different modifications of the studied experimental F3 flame studied in reference [26] by the same author, and all of them were performed using Ansys Fluent. Additional information about the employed CFD methodology can be found in section “2.1. Computational Fluid Dynamics (CFD) methodology”.

As explained in section “3.1. CFD simulations validation and information”, the Navier-Stokes equations were used in their RANS (Reynolds Averaged) form. The K-Epsilon model, being used with $K_{\varepsilon 2} = 1.87$ (as proposed by Jeng and Faeth [69]), was found as the model that provided better results for this case, as was found after having performed a screening of turbulence models, as explained in section “3.1. CFD simulations validation and information”.

The fluid domain that was employed in this article is bidimensional and axisymmetric. It extends 90R in the direction of injection and 61R in the radial direction. R is the radius of the injector in the F3 test case. Accordingly, the mesh used is axisymmetric.

The mesh used for the shown calculations is structured and contains 172,500 nodes. It is markedly refined in radial and axial directions approaching the fuel-oxygen injector. Its minimum cell area is equal to 2.113E-8 m2. It has a minimum orthogonal quality parameter equal to 9.999E-1. The best value of this parameter that could have been

Table 1
Specifications of some electricity production-oriented gas turbines. Source: [72] and catalogs of the manufacturers.

Manufacturer	Model	Power, MW	Pressure Ratio
Centrax	Trent 60 DLE	53	33:1
Centrax	RB211	32	21:1
GE	LM6000PC	46	29.6:1
GE	LMS100	98	40:1
Mitsubishi	M501J	330	23:1
Siemens	SGT-800	47	19:1
Siemens	SGT5-8000H	400	19.2:1
Pratt & Whitney	FT4000 SWIFTPAC 60	68.7	36.7:1
Pratt & Whitney	FT8 SWIFTPAC 25 DLN	25.5	19.5:1

obtained would have been a value equal to 1.

Mesh independency was studied for the air-co-flow case in the following reference by the same author [26]. For this purpose, the procedure proposed by Celik et alia [73] was used.

Spatial discretization was carried out through second-order upwind schemes. The Green-Gauss node-based method [74 75] was used to calculate gradients.

Convergence was determined through two different criteria. The first one assures the stability of some magnitudes, such as the average domain temperature or the average temperature at the outlet. The second one studies the value of certain residuals, ensuring that they are below established thresholds. These thresholds were 10^{-6} in the case of the energy equation and 10^{-5} in the remainder of the other cases.

For the velocity and the turbulent kinetic energy, the experimental profiles calculated for the F3 flame by Chen et alia, included in reference [67], were used as boundary conditions at the fuel-oxygen inlet. The diameter of this injector was also reduced to provide the same amount of fuel as the F3 flame in atmospheric conditions. To apply these boundary conditions to the new reduced diameter of the injector, nondimensional experimental profiles are taken. The turbulent dissipation rate profile was calculated using the turbulent kinetic energy, as proposed by Versteeg et alia [76]. The rest of the turbulence magnitudes had to be estimated as proposed by Versteeg et alia [76].

The average velocity at the fuel-oxygen inlet is 30 m/s. The average speed at the co-flow inlet is 1.59 m/s to provide as similar conditions as possible to the experimental test case.

A summary of the turbulence and velocity boundary conditions is provided in Table 2.

The studied operating pressures, taken from Table 1, are described below:

- 21 atm (21.28 bar). This working pressure can be found in the gas turbine model RB211 by Centrax. This value would represent the lowest range of operating pressures.
- 30 atm (30.4 bar). This operating pressure can be found in the model LM6000PC by General Electric. This value would represent the medium range of operating pressures.
- 40 atm (40.53 bar). This operating pressure can be found in the LMS100 by General Electric. It would represent the high range of operating pressures.

Table 3 shows a summary of the previously described CFD operating pressures.

With respect to the domain's pressure loss, it was taken into account that the fluid domain represents the internal part of a combustion chamber. In this way, the pressure losses that come from that part of the combustion chamber should only be taken into account, without considering other losses that could come, for example, from its inlet. Accordingly, the data contained in the following reference [77] could be applied. Thereby, considering the length of the fluid domain, a value of 0.985 for P_{exit}/P_{inlet} was taken.

With respect to the temperatures at the inlets, they were selected as follows:

- Fuel inlet: a stoichiometric mixture of methane and oxygen is injected into this location. To select the temperature at this point, it should be taken into account how the oxygen is produced. For this purpose, an Air Separation Unit (ASU) is typically employed [78]. These devices use technologies that range from the already developed cryogenic technologies to ion transport membranes [79]. As has been shown, it should be covered this way a wide range of different technologies. A temperature of 298 K for this inlet was taken in an attempt to cover all the various possibilities available.
- Co-flow inlet: to reduce additional noises, a temperature of 800 K was taken for all the different cases studied. This temperature would be the one obtained when compressing air starting from 298 K to the desired operating pressures with a compressor efficiency equal to 0.9.

Table 2
Oxy-combustion turbulence and velocity boundary conditions.

	Velocity m/s	Kinetic energy	Dissipation rate
Inlet Fuel	Experimental [67]	Experimental [67]	Calculated [67 76]
Inlet Co-flow	1.59	Estimated [76]	Estimated [76]

Table 3
Summary of the studied CFD operating pressures.

	Studied CFD operating pressures
Operating pressure 1	21 atm (21.28 bar)
Operating pressure 2	30 atm (30.4 bar)
Operating pressure 3	40 atm (40.53 bar)

Regarding the compositions at the inlets, the fuel-oxygen mixture is supplied in stoichiometric conditions at the main injector. In what respects to the co-flow composition, the following were studied:

1) Air: Although this case is not be found in semi-closed CO_2-capturing devices, it is an important case to study because it represents a reference case. Its importance comes from the fact that it allows a comparison with performing combustion in conventional gas turbines. Although it could have been possible in this case to perform a diffusion flame, taking the required oxygen from the co-flow, it was not how combustion was studied. The needed oxygen to carry out the chemical reactions was supplied with the fuel in a premixed way to allow a comparison with the semi-closed cases.
2) 100% CO_2: This case was considered representative of those cycles in which a carbon-based flow is used as a working fluid (this type of cycle recirculates flows mainly composed of carbon dioxide).
3) 100% H_2O: this case was taken as representative of the working fluid composition in water cycles.

4. Oxy-combustion CFD flow field results

4.1. Temperature results

The effect of the operating pressure and the co-flow composition on the temperature field is analyzed in this section. To further check the temperature fields obtained for the target oxy-combustion cases, a simplified simulation was also performed to check the maximum temperature obtained in atmospheric conditions. This simplified case consisted of a methane-oxygen flame in atmospheric conditions inside an air co-flow initially entering the domain at 298 K. The same boundary conditions as shown in Table 2 were applied in this case. A maximum temperature equal to 3046.4 K was obtained for this case. This amount was consistent with the experimental studies performed by Oh [80].

Fig. 3 shows the obtained temperature field for the studied co-flows along the symmetry axis. This axis contains the position of the injector (x/d = 0) and the injection direction.

As shown in Fig. 3, the temperature evolution does not differ in the first part of the axis, being the maximum temperature obtained the same in the three studied cases. It should be noted that all the cases perform oxy-combustion in premixed conditions, being the required oxygen provided along with the fuel. The length of the maximum temperature zone varies from one case to another. The case that presents the most extensive high-temperature zone is the air co-flow case. The case that shows the smallest high-temperature location is the CO_2 co-flow case. The water co-flow case shows an intermediate behavior compared to the first-mentioned cases.

After the maximum temperature zone, temperatures start decreasing in the flame trails. The air co-flow case shows the highest temperatures

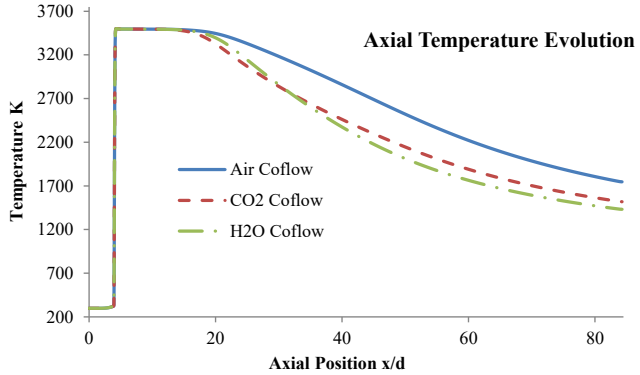

Fig. 3. Axial Temperature Evolution, 30 atm.

of the studied cases in the trail. In the first part of the trails, the H_2O co-flow case shows higher temperatures in comparison with the carbon dioxide case.

After this initial part of the trails, the temperature in the H_2O co-flow case starts decreasing faster than the temperature in the CO_2 case. In the final part of the trails, the air co-flow presents the highest temperatures of the studied cases. The H_2O co-flow case shows the lowest temperatures of the studied cases, being its temperatures lower than the temperatures of the CO_2 case.

As explained in [26], although the maximum temperature obtained in oxy-combustion is higher than when performing conventional combustion with air, the temperature reduction obtained with the new working fluid composition in semi-closed cycles would help turbines to work at a more appropriate temperature range.

Fig. 3 shows that recirculating a water-based flow instead of a carbon-based flow would help turbines work in an even more appropriate temperature range. Thereby, and from the point of view of the working of the turbines, it would be desirable to recirculate a water-based fluid instead of a carbon-based fluid. This would also allow the construction of shorter combustion chambers to obtain a desired temperature level.

Figs. 4 and 5 contain the temperature evolution in the perpendicular direction to the symmetry axis when performing combustion at 30 atm (30.4 bar) pressure.

When comparing the different x/d positions shown in Fig. 4 and Fig. 5 among them, it can be noticed:

- For all the studied co-flows, in the first three x/d positions, shown in Fig. 4, the obtained temperatures on the symmetry axis (x/d = 0) and near it are the same for the three studied co-flows. After the three x/d positions in Fig. 4, the temperatures on the symmetry axis and near it progressively decrease.

The air co-flow case shows higher temperatures than the CO_2 case and the H_2O case, except for those positions where temperatures are the same for the three studied cases. These higher temperatures in the air co-flow case happen again near and at the outlet. Lower temperatures were also found by Li et alia [81] when diluting combustion, in that case with carbon dioxide.

- The extension of the zones where all the studied cases have the same temperature is reduced when separating from the injector for all the studied cases.
- In terms of temperature, the extension of the flame trails becomes bigger when approaching the outlet. This happens for all the studied co-flows.

When comparing the different co-flows among them, it can be found as follows:

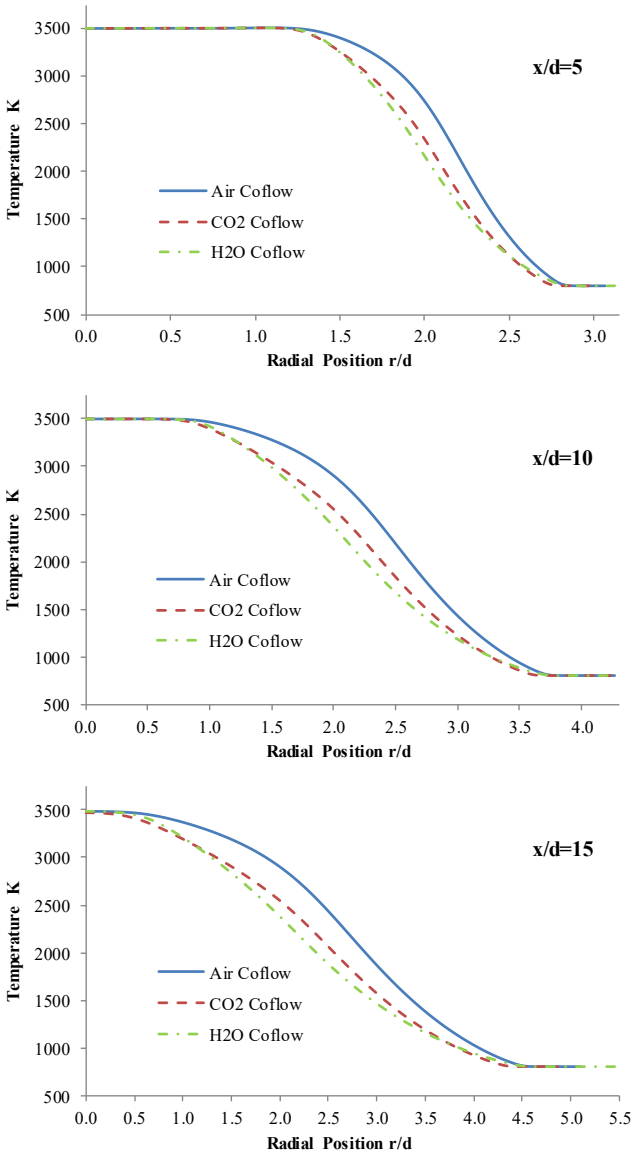

Fig. 4. Evolution of temperature in the direction perpendicular to the symmetry axis, 30 atm.

- Except for those positions where all the studied cases present the same temperatures, the air co-flow is the case in which the temperatures are the highest ones.
- In positions x/d = 0 to x/d = 20, in the points near the symmetry axis and except for those locations where all the cases present the same temperatures, the H_2O co-flow presents higher temperatures than the CO_2 co-flow.
- In the flame trail edges, whatever position is analyzed, the H_2O co-flow presents higher temperatures than the CO_2 co-flow. The air co-flow would be the case with the highest temperatures in these locations.
- Except for the previously exposed points, the H_2O co-flow presents lower temperatures than the CO_2 co-flow, being the air co-flow the case with the highest temperatures.

4.1.1. *Pressure effect*

Figs. 6 to 8 show the pressure effect on the temperature field along the symmetry axis. Increases in the operating pressures are directly translated into increases in the obtained temperatures. Along with that,

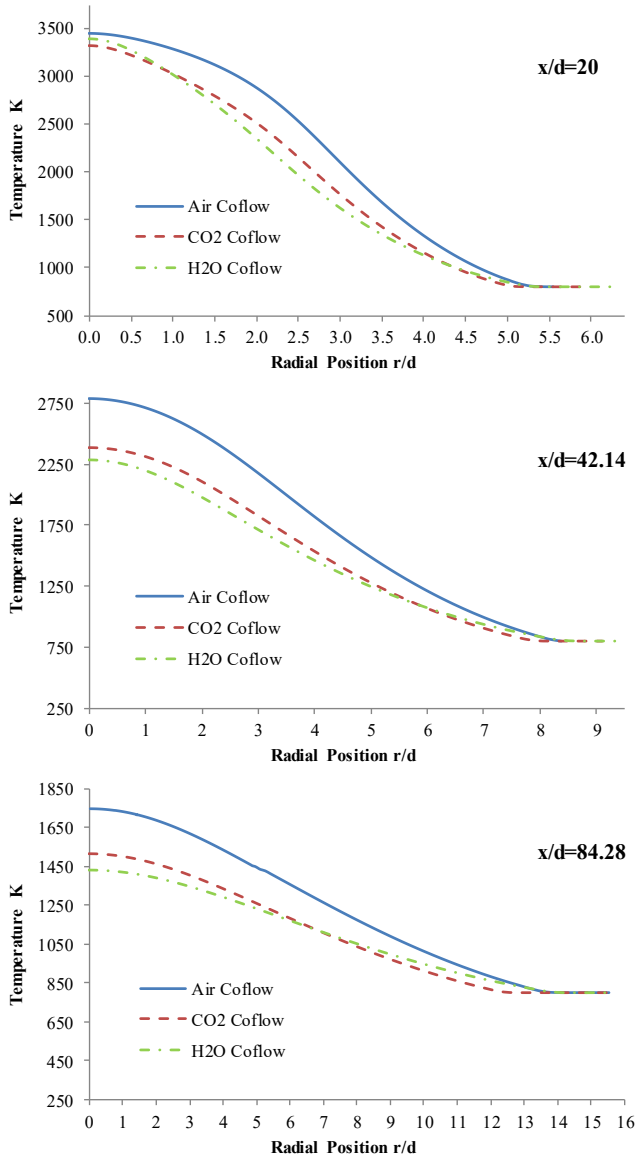

Fig. 5. Evolution of temperature in the direction perpendicular to the symmetry axis, 30 atm.

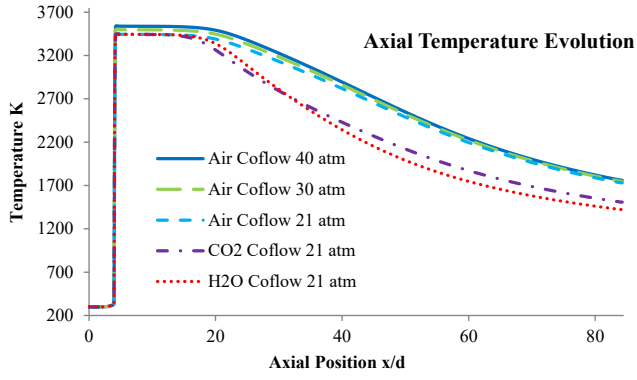

Fig. 6. Temperature evolution along the symmetry axis, H_2O and CO_2 co-flows 21 atm, Air co-flow 21 to 40 atm.

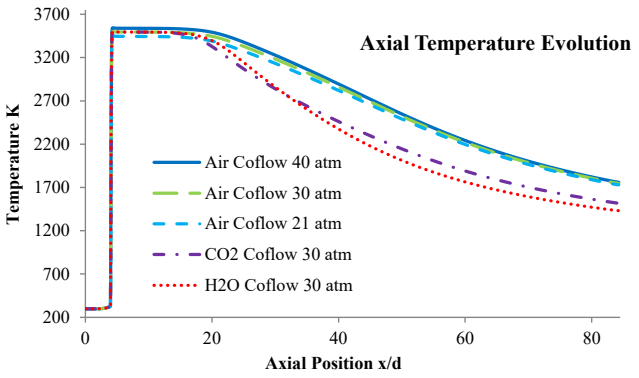

Fig. 7. Temperature evolution along the symmetry axis, H_2O and CO_2 co-flows 30 atm, Air co-flow 21 to 40 atm.

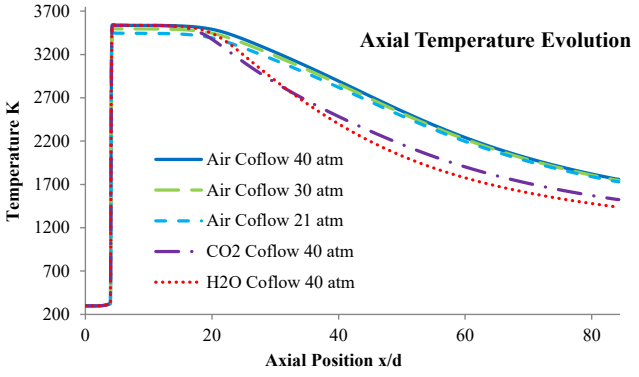

Fig. 8. Temperature evolution along the symmetry axis, H_2O and CO_2 co-flows 40 atm, Air co-flow 21 to 40 atm.

the maximum-temperature zone also extends its size when increasing the working pressure (this fact can be more easily noticed when comparing the 21 atm, 21.28 bar, cases to the 40 atm, 40.53 bar, cases).

All the studied co-flows present the same temperature evolution near the fuel injector (x/d = 0). It is not until the fuel-oxygen mixture (injected in the main injector) starts mixing with the surrounding co-flows that noticeable differences can be found. Along with the temperature increases when increasing the operating pressures, it can be noticed that the H_2O and CO_2 co-flows decrease the flow temperature along the symmetry axis faster than the Air co-flow whatever operating pressure is considered.

When comparing the H_2O co-flow and the CO_2 co-flow, remarkable differences in their behaviors can be noticed. Whatever operating pressure is considered, the H_2O co-flow keeps higher temperatures than the CO_2 co-flow farther from the injector (higher x/d positions). After that part where the H_2O co-flow presents higher temperatures than the CO_2 co-flow, both cases reach the same temperatures. After that, the H_2O co-flow descends the obtained temperatures faster than the CO_2 co-flow. As said above, this fact happens whatever operating pressure is considered.

Figs. 9 and 10 show the pressure effect on the temperature field for the H_2O co-flow. As can be noticed, higher operating pressures are directly translated into higher temperatures. This fact is especially noticeable near the fuel injector. Although it is also detected in those positions far from the injector, this fact is much more softened.

Increases in the operating pressure are also translated into more extensive high-temperature zones. This fact is especially noticeable when comparing the 21 atm case to the 40 atm case (21.28 to 40.53 bar). It can also be more readily appreciated in those positions close to the injector (x/d = 0).

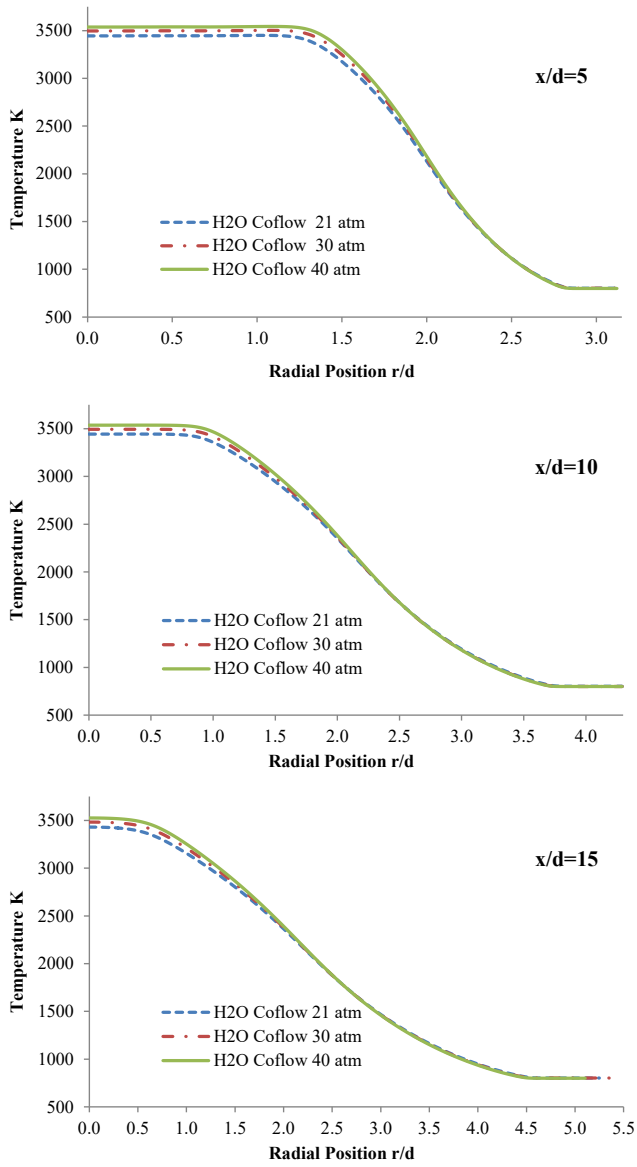

Fig. 9. Evolution of temperature in the direction perpendicular to the symmetry axis, H_2O co-flow, and various pressures. Positions close to the fuel-oxygen injector.

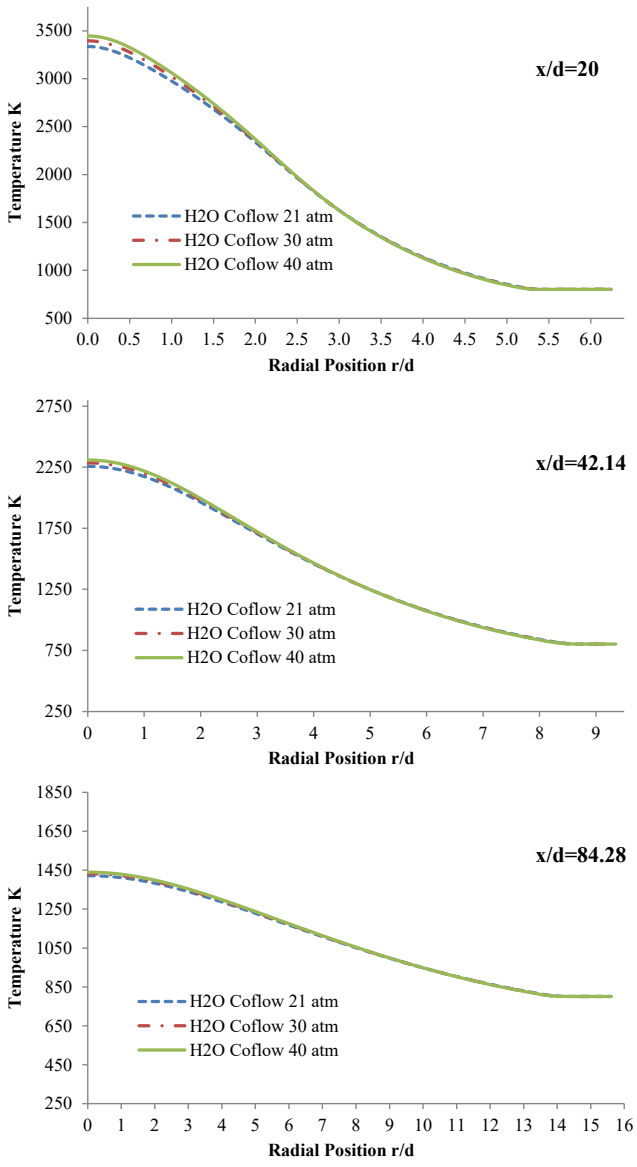

Fig. 10. Evolution of temperature in the direction perpendicular to the symmetry axis, H_2O co-flow, and various pressures. Positions far from the fuel-oxygen injector.

The temperature differences that can be found between the studied operating pressures are more noticeable near the fuel injector. In those positions far from the fuel injector, the temperature differences when changing the operating pressure are much more softened.

When comparing Fig. 9 to Fig. 10, it can be noticed that whatever operating pressure is considered, the size of the flame trail (from a temperature point of view) grows when separating from the injector (x/d = 0). As mentioned above, it can also be noticed how the differences between the studied cases are softened in those positions far from the fuel injector (x/d = 0).

4.2. Turbines' inlet conditions

Generally speaking, power cycles have a turbine stage right after the combustion chambers (if there would be more than one). In the provided diagram of water cycles shown in Fig. 1, there are two turbine stages right after each combustion chamber.

Turbines have a significant impact on the cycle's performance since they move the compression stages and the electric generator. Accordingly, any difference found in their inlets would directly affect the overall work of the gas turbine and the electric generator.

In this section, it is analyzed the differences that may be found at the turbine-stage inlet when performing oxy-combustion inside a water-based environment in comparison to a carbon-based environment. The results of performing oxy-combustion inside an air-based environment are also shown as a reference case. Comparing all these cases between them gives a good idea of the strong points and weaknesses of choosing a recirculating flow or another.

As was shown in section 4.2.1, the main factor that affects the fluid field inside the combustion domain is the co-flow composition. The pressure effect is secondary in comparison to the impact of the co-flow composition. Considering the previous fact, only the obtained results for a pressure of 30 atm (30.4 bar) are shown in the section.

4.2.1. Density

Fig. 11 shows the obtained density values at the outlet of the combustion domain. It can be noticed how, for all the studied cases, the obtained densities at the flame trails are lower than the obtained

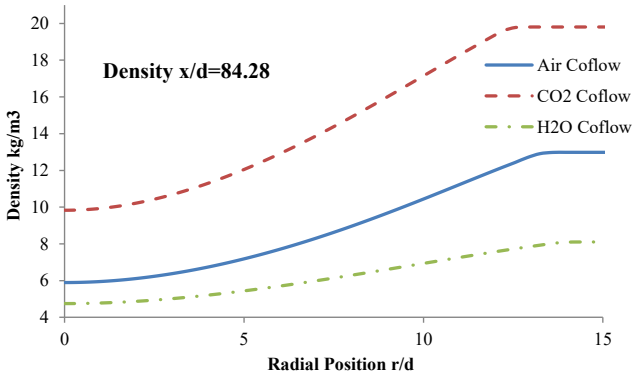

Fig. 11. Turbine Inlet Density, 30 atm.

densities in the unaltered co-flows. The obtained values depend not only on the molecular weight of the fluid at the presented locations but also on the obtained temperatures at the presented points.

As can be noticed, the case that shows the highest density values is the CO_2 co-flow. The case with the lowest density values is the H_2O co-flow. Meanwhile, the conventional air co-flow shows intermediate values (although closer to the H_2O ones) between the CO_2 co-flow and the H_2O co-flow.

4.2.2. Sound speed

Fig. 12 shows the obtained sound speed values at the outlet of the combustion domain. In this magnitude, the most important differences are found between recirculating carbon-based co-flows and water-based co-flows.

The CO_2 co-flow presents much lower sound speeds in comparison with the conventional air co-flow. In the following reference by the same author [30], these lower sound speed values were found as one of the main problems, among others, of carbon-based co-flows. In that work, the reuse of a modern LPT, designed to work with air and remains of combustion, was studied when employing a carbon-based fluid from a semi-closed Brayton cycle. One of the main problems was that the LPT easily became sonic, and its efficiency decreased drastically.

The H_2O co-flow, however, shows much higher sound speed values at this location. These values are even higher than the ones of the conventional air co-flow. This would help the turbines to work avoiding most of the sonic-derived problems.

4.2.3. Axial velocity

Fig. 13 shows the obtained axial velocity values at the turbine stage inlet. Only the axial values are shown because the rest of the components are negligible in this location.

As can be noticed, the CO_2 co-flow presents the lowest axial velocity values. The H_2O co-flow, however, shows the highest axial velocity values of the three considered cases, its values slightly higher than the air co-flow case. Although the CO_2 co-flow presents the lowest velocity values, it should also be reminded that its sound speed at this location is much lower than in the rest of the cases.

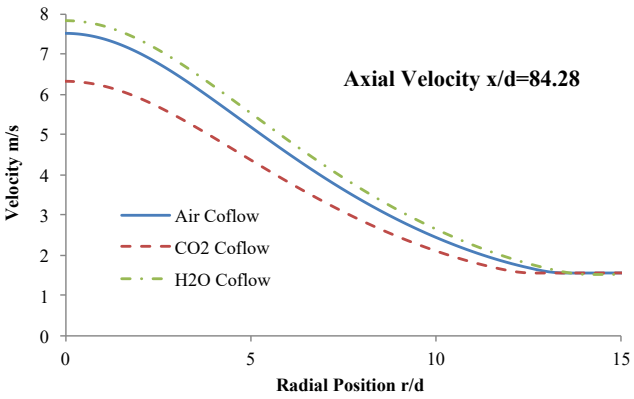

Fig. 13. Turbine inlet axial velocity, 30 atm.

4.2.4. Temperature

The temperature field at the inlet of the HPT was shown in Fig. 5, position x/d = 84.28. In that figure, it can be noticed how the Air co-flow presents much higher temperatures in this position when compared to the H_2O or the CO_2 co-flow cases. This temperature reduction in this position when employing fluids with a high concentration of CO_2 in their composition was also found experimentally by Best et alia [82]. In that work, instead of performing an oxy-combustion semi-closed Brayton cycle, a micro gas turbine was studied when injecting carbon dioxide at its inlet.

When comparing the H_2O co-flow to the CO_2 co-flow, it can be noticed how the CO_2 working fluid presents higher temperature values than the H_2O one. Despite this fact, when analyzing the available energy at the outlet of the combustion domain, the specific heat Cp has to be considered.

Fig. 14 shows the specific heat Cp at the outlet of the combustion domain for all the studied co-flows in the 30 atm (30.4 bar) operating pressure case. As can be noticed, although the CO_2 co-flow and the H_2O co-flow present lower temperatures in this position when compared to the Air co-flow, these two cases present higher Cp values in this position. In this way, the possibility of adding heat recovery systems at some point in the cycles should be carefully considered in these two cases. This fact is usually taken into account in the water cycle with a heat recovery steam generator.

When comparing the CO_2 co-flow to the H_2O co-flow, Fig. 14 clearly shows one of the most remarkable differences between the H_2O co-flow

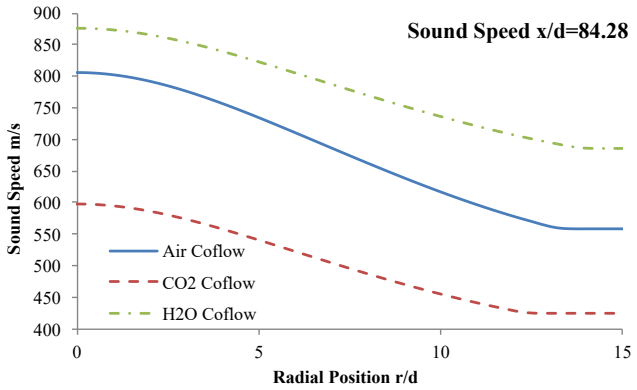

Fig. 12. Turbine Inlet Sound Speed, 30 atm.

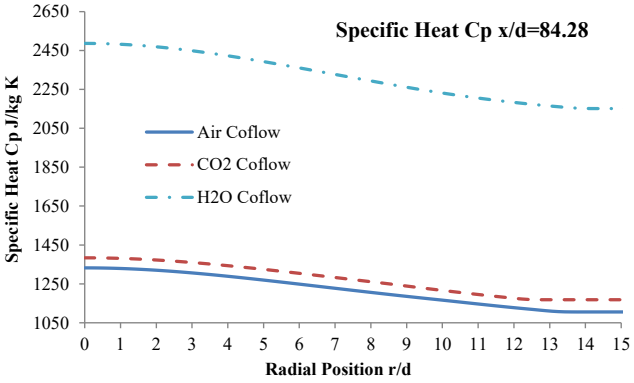

Fig. 14. Turbine inlet Cp values, 30 atm.

and the CO_2 co-flow. The H_2O co-flow presents much higher Cp values in this position when compared to the CO_2 co-flow. In that sense, it can almost be said that the CO_2 co-flow has more similar Cp values to the conventional air working fluid than to the H_2O one.

Some of the main differences found between employing carbon-based working fluids and water-based ones at the inlet of the turbine stage are listed below.

- Carbon-based working fluids have higher densities in comparison with a conventional air working fluid. Concerning water-based fluids, their densities are slightly lower than the values obtained with a conventional air working fluid.
- Carbon-based fluids have much lower sound speeds in comparison to air. Water-based fluids, however, have higher sound speeds in comparison to air. This would sort out some of the main problems in the turbines when working with carbon-based fluids [30].
- Water-based fluids would have slightly higher velocity values at the turbine's inlet when compared to a conventional air fluid. Carbon-based fluids would have slightly lower velocity values in this location when compared to a conventional air fluid.
- Water-based fluids have much higher Cp values in this location than carbon-based fluids and conventional air.

5. Performance analysis study of recycling CO_2 and H_2O working fluids

In this section, the performance of the carbon-based and water-based dual recuperative cycle (DRC) and reheating cycle (RHC) with the variation of maximum cycle temperature at the inlet of the turbine, state 1, (T_{max}), maximum cycle pressure at the outlet of the compressor, state 7, (P_{max}), and minimum cycle temperature at the inlet of the compressor, state 6, (T_{min}) is analyzed. For the present analysis, the isentropic efficiency of the turbines and compressors are assumed to be 93% and 85%, respectively [83]. In addition, the economic analysis was performed on a plant lifetime of 20 years and a plant utilization factor of 85% [29]. Furthermore, the fuel cost and operating and maintenance costs are set as 0.07 \$/kWh$_e$, and 0.008 \$/kWh$_e$, respectively [29]. The thermophysical properties of the used working fluids at the main state points of the investigated schemes are presented in the supplementary material (Table SM. 3). The thermodynamic properties of these fluids were obtained from the library of the real fluids of the Engineering Equation Solver (EES), which is used for the thermoeconomic analysis of this study. Moreover, the details of the adjustment variables and design parameters limitations are presented in the supplementary material (Table SM. 4).

Fig. 15 shows the relationship between the T_{max} and the thermal efficiency and LCOE of both carbon-based and water-based DRC and RHC at P_{max} of 30.40 bar and T_{min} of 310 K. As T_{max} increases from 1100 K to 1423 K, the thermal efficiency of the carbon-based DRC is improved by 58.62% (increased from 24.63% at 1100 K to 39.07% at 1423 K). For the water-based DRC, the thermal efficiency is improved only by 18.18% (increased from 28.38% to 33.54% over the range of T_{max}). A similar trend is noted for the RHC as the thermal efficiency of the carbon-based configuration is improved by 35.17% and by 14.40% for the water-based configuration. This implies that T_{max} dominates the performance of the carbon-based cycles more than that of the waster-based cycles.

This is explained by the that the specific heat of the CO_2 is lower than that of the water which enhances the temperature of the recycled CO_2 at the inlet of the combustor (which is considered a calculated variable in this section) more than of the recycled water. For instance, at a Pmax of 30.4 bar and temperature of 600 K (at the outlet of the compressor), the specific heat of CO_2 is 1.099 kJ/kg-K which is 54.7 % lower than of the water under the same conditions (2.428 kJ/kg-K). This, in turn, minimizes the amount of the required fuel to reach the desired maximum temperature and yields higher thermal efficiency. As compared in Table 4, the same maximum cycle temperature of 1373 K is achieved at a lower fuel flow rate in carbon-based cycles compared to that of water-based cycles. For example, at T_{max} of 1373 K, the fuel flow rate of the carbon-based RHC is 1.88 kg/s, which is 20.3% lower than of the water-based RHC (2.36 kg/s).

Fig. 15(a) shows that the RHC configurations have higher thermal efficiencies than that of the DRC configurations; thus the average LCOE of the reheating cycles (4.01 ¢/kWh) is lower than that of the dual recuperative cycles (4.47 ¢/kWh) by 10.29%. Furthermore, the

Table 4
Comparison of carbon-based and water-based DRC and HRC cycles at design point conditions*.

Item	Carbon-based		Water-based	
	DRC	RHC	DRC	RHC
Thermal efficiency, [%]	39.39	47.50	33.54	39.87
LCOE, [¢/kWh]	4.35	3.96	4.34	4.04
Gross turbine power, [MW]	104.81	88.84	50.13	50.09
Compression power, [MW]	54.81	38.84	0.13	0.095
Recuperative heat, [MW]	70.49	92.07	33.65	44.35
Precooler load, [MW]	77.41	54.86	95.67	69.15
Total fuel flow, [kg/s]	2.38	1.88	2.66	2.36
Recycled flow, [kg/s]	187.3	135.1	30.94	23.25

*T_{max} = 1373 K, P_{max} = 30.4 [bar], PR = 20, T_{min} = 310 K, and P_{net} = 50 MW.

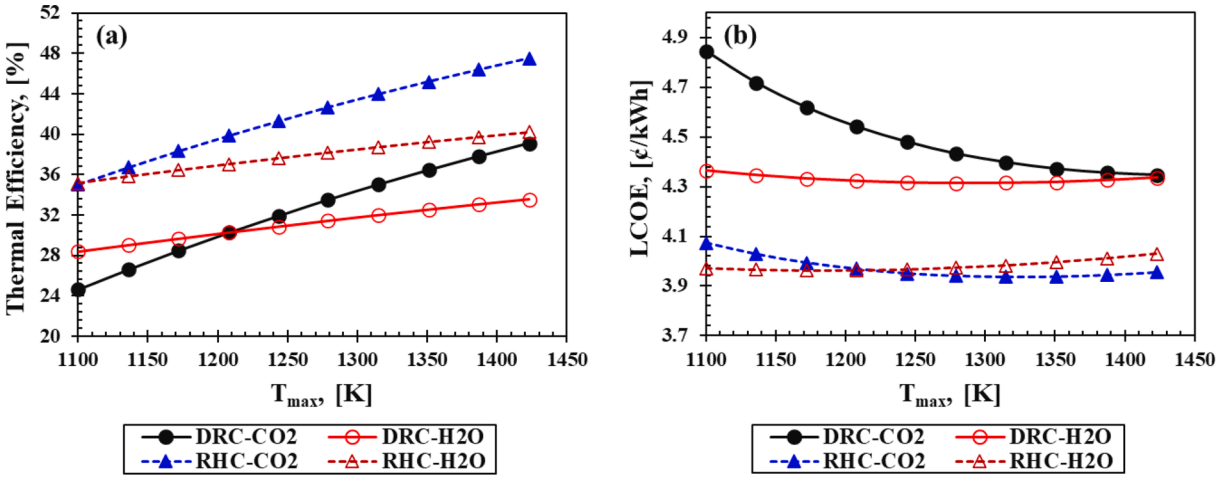

Fig. 15. Effect of maximum cycle temperature on the (a) thermal efficiency, and (b) LCOE of the carbon-based and water-based DRC and RHC at P_{max} of 30.40 bar and T_{min} of 310 K.

compression power of the water-based cycles is much lower than that of the carbon-based cycles as shown in Table 4 at the design point conditions. Therefore, the average LCOE of the water-based DRC (4.35 ¢/kWh) is lower than that of the carbon-based DRC (4.47 ¢/kWh) by an average of 2.68%. However, for the reheating configurations, the LCOE of the water-based cycle is lower than that of the carbon-based cycle at T_{max} lower than 1208 K as shown in Fig. 15(b). But, at Tmax higher than 1208 K, the improvement achieved in the thermal efficiency of the reheating carbon-based cycle affects its LCOE more than the reduction of the compression power of the water-based cycle. Therefore, the reheating carbon-based cycle achieves the minimum LCOE at T_{max} higher than 1208 K.

In contrast to the maximum cycle temperature, the maximum cycle pressure (P_{max}) slightly changes the performance of the investigated cycles from energetic and economic points of view. As shown in Fig. 16 (a), the thermal efficiency of the studied configurations is improved by an average of 1.36% for the dual recuperative cycles and by 0.63% for the reheating cycles (for both carbon-based and water-based cases). This is because the turbine work slightly increases with the increase of P_{max} at a constant pressure ratio (PR = 20). Similar to the thermal efficiency, the LCOE slightly reduces over the range of P_{max} (as shown in Fig. 16(b)) by an average of 0.52% in dual recuperative cycles and by 0.25% in reheating cycles.

If the maximum cycle pressure is fixed and the minimum cycle pressure (P_{min}) is changed from 1.5 bar to 5 bar, the thermal efficiencies and the LCOE of the investigated configurations will be as shown in Fig. 17. In general, it is noticed that with the increase of P_{min}, the efficiency of the DRC configurations is increased and the RHC is decreased. This implies that lower minimum cycle pressure is advantageous for the reheating configurations. However, for the reheating carbon-based configuration, the efficiency slightly increases as P_{min} reduces from 5 bar to 3 bar. Further decreases in P_{min} yield lower efficiency than the optimum achieved at 3 bar. This is explained that for reheating configurations, lower P_{min} enables larger expansion work for the second turbine which is more than the additional power required for the compression process. However, from an economic point of view, lower P_{min} in reheating configurations slightly reduced the LCOE of the water-based compared to the carbon-based configurations. At the optimum P_{min} (3 bar), the LCOE of the carbon-based reheated cycle is 0.60 % lower than at P_{min} of 5 bar.

The minimum temperature of the cycle depends on the precooling process conditions which are categorized as: (a) Dry-cooling where air fans are used for the precooling process which yields a minimum temperature between 313 K and 323 K, and (b) Wet-cooling where the water-cooling tower is used which provides minimum temperature less than 310 K. While lower T_{min} (wet-cooling) is considered more expensive than the dry-cooling (in terms of capital cost), it enhances the thermal efficiency of carbon-based cycles more than of the water-based cycles as shown in Fig. 18(a). However, the thermal efficiency of the water-based cycles slightly changed over the range of T_{min}. Moreover, the LCOE of the carbon-based RHC is the minimum (3.92 ¢/kWh) at T_{min} of 305 K (wet cooling) and identical to the water-based RHC (4.00 ¢/kWh) at T_{min} of 323 K (dry-cooling). Thus, for DRC, the water-based cycle is economically more preferred than the carbon-based cycle under the mentioned conditions in this study. For the RHC, the carbon-based cycle is the best from both energetic and economic perspectives.

An energetic and economic comparison between the investigated recuperative and reheating carbon-based and water-based cycles in this study with other semi-closed Brayton cycles available in the literature is presented in Table 5. It can be noted that the thermal efficiency of the present cycles that work at Pmax lower than 41 bar is lower than that works at supercritical pressure level (supercritical carbon dioxide (sCO_2) Brayton cycles with P_{max} higher than 200 bar). However, the capital costs of the sCO_2 cycles are still much higher than that of the gas Brayton cycles that work at P_{max} less than 41 bar. Therefore, the present configuration is considered a promised solution to capture CO_2 emissions with significant cost savings compared to the sCO_2 cycles. However, further improvement in their energetic performance is needed.

6. Conclusions

As fossil fuels still form the primary source of worldwide energy alongside the increase of their negative impacts on the environment such as global warming and ozone depletion issues, the development of new fossil-fuel-based technologies with near-zero emissions is urgent. This study investigates the application of carbon-based and water-based oxy-combustion power cycles for power generation at a feasible operating pressure of less than 42 bar. This ensures the fast development of these cycles as the technology of the various cycle components at such pressure is already mature and commercialized for the gas power plants. The methodologies employed comprise CFD analysis of reacting flows as well as performance analysis methods. This would allow a better knowledge of the overall performances of the resulting cycles as well as gaining insight into the phenomenology in these devices' combustion chambers and at the inlet of their turbine stages. It studied as well the effect of employing one or two combustion chambers (reheating). The main conclusions of the present study can be summarised as follows:

- From the combustion analysis study, it was found that water-recycling cycles present a more important temperature abatement

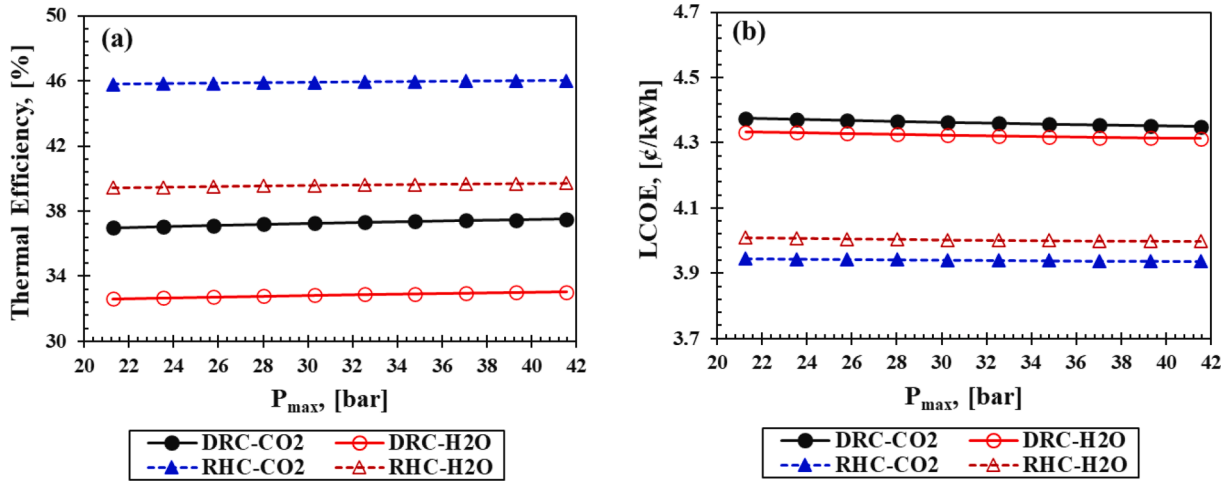

Fig. 16. Effect of maximum cycle pressure on the (a) thermal efficiency, and (b) LCOE of the carbon-based and water-based DRC and RHC at T_{max} of 1373 K, T_{min} of 310 K, and constant pressure ratio (PR = 20).

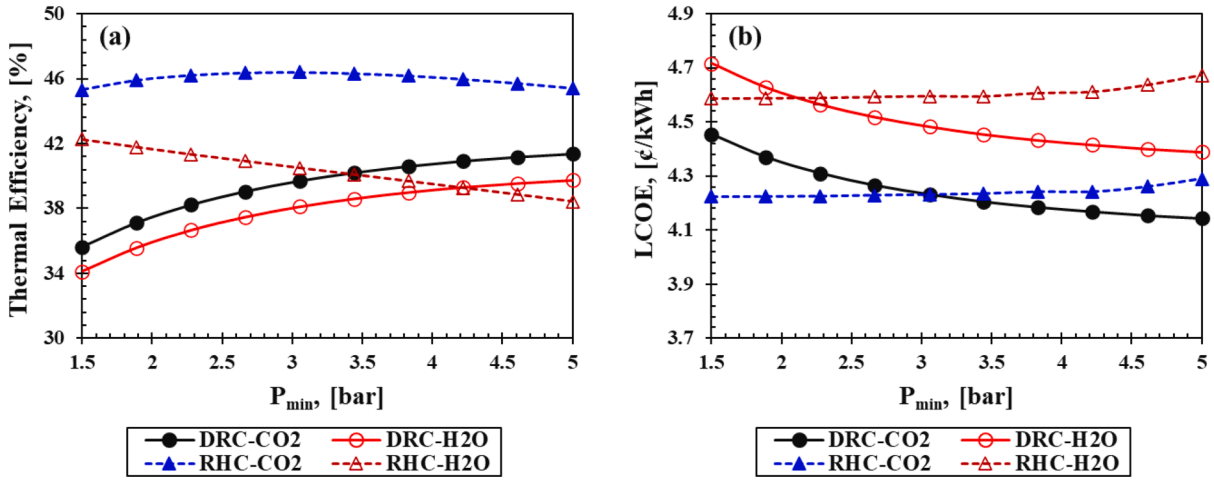

Fig. 17. Effect of minimum cycle pressure on the (a) thermal efficiency, and (b) LCOE of the carbon-based and water-based DRC and RHC at T_{max} of 1373 K and T_{min} of 310 K.

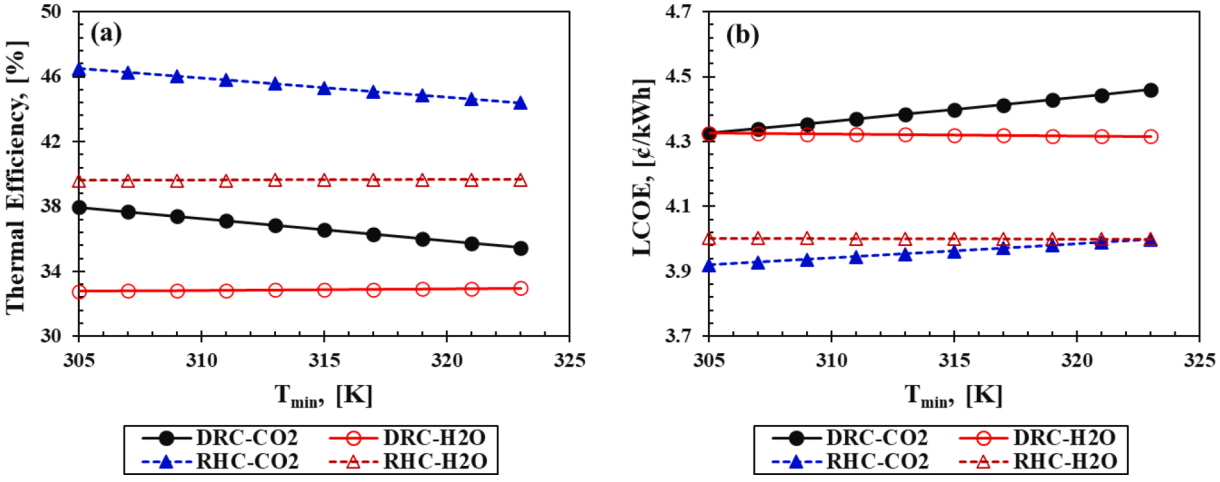

Fig. 18. Effect of minimum cycle temperature on the (a) thermal efficiency, and (b) LCOE of the carbon-based and water-based DRC and RHC at P_{max} of 30.4 bar and T_{max} of 1373 K.

Table 5
Comparison of the present cycles with other cycles available in the literature.

Cycle configuration	Thermal efficiency, [%]	LCOE, [¢/kWh]	Reference
Carbon-based DRC	39.39	4.35	This work
Supercritical carbon-based DRC	45.65	5.386	[65]
Carbon-based RHC	47.50	3.96	This work
Supercritical carbon-based RHC	49.32	Not provided	[29]
Water-based DRC	33.54	4.34	This work
Water-based RHC	39.87	4.04	This work
Integrated gas turbine + Supercritical carbon-based power cycle + ORC	52.10	5.28	[66]

than the CO_2-recycling ones. This can be found on the combustion domain's symmetry axis and in its perpendicular direction, in the flame trail part close to this axis (except for those points where temperatures are the same). The only exception would be in those points farther from the symmetry axis, where water-recycling cycles present slightly higher temperatures than the CO_2-recycling ones.

- Both CO_2-recycling and H_2O recycling cycles present lower temperatures in the flame trail than performing oxy-combustion in a conventional air environment. This higher temperature abatement in H_2O-recycling cycles than in the CO_2-recycling ones could be an interesting feature in case overheating phenomena would be detected in these oxy-combustion cycles.
- From an aerodynamic point of view, water-recycling cycles present higher sound speed values than air cycles and are especially much higher than the CO_2-recycling ones. This would be an important feature since one of the main problems of CO_2-recycling cycles is that the turbines easily become sonic. These sonic zones lead to a drop in the efficiency of these components and a subsequent malfunctioning or even unavailability, as was found by the same author when studying a real Low-Pressure Turbine in CO_2-recycling conditions [30].
- From the performance analysis carried out, it was found that the thermal efficiency of the carbon-based DRC cycle is improved by 58.62% as the maximum cycle temperature increased from 1100 K to 1432 K, compared to 18.18% of the water-based DRC cycle. At the same temperature range, the thermal efficiency of the RHC is improved by 35.15% for carbon-based and 14.40% for water-based configurations.

- Maximum efficiency of 47.50% is obtained by the CO_2-based RHC at the wet-cooling conditions and a minimum cycle efficiency of 33.54% is obtained by the water-based DRC at dry-cooling conditions.
- From the economic analysis point of view, it was found that the capital costs of the supercritical carbon-based (sCO_2) cycles or integrated gas-turbine cycles are much higher than of the present carbon-based and water-based cycles. This is mainly caused that the present cycles operated at maximum pressure less than of 42 bar compared to a minimum of 200 bar in sCO_2 cycles.
- The simplicity of the present cycles avoids the additional capital costs of the integrated cycles as the ORC in the gas-turbine-based cycles. Therefore, the average LCOE of the present carbon-based and water-based cycles is 3.859 ¢/kWh, which is 28% lower than the average LCOE of the supercritical carbon-based and integrated gas-turbine based cycles.

While the present study proves the technical and thermoeconomic feasibility of the carbon-based and water-based oxy-combustion power cycles compared to the supercritical carbon-based cycles, further investigations are needed in future work to have detailed insight into their features and limitations compared to the available technologies in the literature. These investigations include exergy analysis, exergoeconomic analysis, optimization analysis, environmental analysis, and life cycle assessment.

Declaration of Competing Interest

The authors declare that they have no known competing financial interests or personal relationships that could have appeared to influence the work reported in this paper.

Acknowledgments

The authors are grateful to Universidad de León, Qatar University, and Drotium for their help in the completion of this study and publication

Appendix A. Supplementary material

Supplementary data to this article can be found online at https://doi.org/10.1016/j.applthermaleng.2022.119296.

References

[1] Y. Qureshi, U. Ali, F. Sher, Part load operation of natural gas fired power plant with CO2 capture system for selective exhaust gas recirculation, Appl. Therm. Eng. 190 (2021) 116808, https://doi.org/10.1016/j.applthermaleng.2021.116808.
[2] UNFCCC, Kyoto protocol to the United Nation framework convention on climate change, 1997. Available from: <http://unfccc.int>.
[3] UNFCC, UNFCC Paris Agreement, UNFCC. 45 (2015).
[4] United Nations, COP26 THE GLASGOW CLIMATE PACT, (2021).
[5] EEA (European Environment Agency), Annual European Union greenhouse gas inventory 1990-2019 and inventory report 2021, n.d.
[6] U.S. EPA, Inventory of U.S Greenhouse Gas Emissions and Sinks. EPA 430-R-21-005, Environmental Protection Agency. (2021).
[7] A. Arroyo, P. Castro, M. Manana, R. Domingo, A. Laso, CO2 footprint reduction and efficiency increase using the dynamic rate in overhead power lines connected to wind farms, Appl. Therm. Eng. 130 (2018), https://doi.org/10.1016/j.applthermaleng.2017.11.095.
[8] IEA, Statistics report. Key World Energy Statistics 2020, 2020.
[9] T.M. Gür, Carbon dioxide emissions, capture, storage and utilization: review of materials, processes and technologies, Prog. Energy Combust. Sci. 89 (2022) 100965.
[10] R. Zhai, J. Qi, Y. Zhu, M. Zhao, Y. Yang, Novel system integrations of 1000 MW coal-fired power plant retrofitted with solar energy and CO2 capture system, Appl. Therm. Eng. 125 (2017), https://doi.org/10.1016/j.applthermaleng.2017.07.093.
[11] J. Gomes, S. Santos, J. Bordado, Choosing amine-based absorbents for CO2 capture, Environ. Technol. (United Kingdom). 36 (1) (2015) 19–25.
[12] C. Zhou, Y. Yu, C. Zhang, J. Zhang, Z. Zhang, G.G.X. Wang, CO2 capture intensified by solvents with metal hydride, Fuel Process. Technol. 218 (2021) 106859, https://doi.org/10.1016/j.fuproc.2021.106859.
[13] R.V. Barrulas, M. Zanatta, M.C. Corvo, Porous ionic liquid derived materials for CO2 emissions mitigation, Eng. Mater. (2022), https://doi.org/10.1007/978-3-030-85397-6_20.
[14] R.V. Barrulas, C. López-Iglesias, M. Zanatta, T. Casimiro, G. Mármol, M.R. Carrott, C.A. García-González, M.C. Corvo, The AEROPILs generation: novel poly(ionic liquid)-based aerogels for CO2 capture, Int. J. Mol. Sci. 23 (1) (2022) 200, https://doi.org/10.3390/ijms23010200.
[15] S. Son, J.Y. Heo, N.I. Kim, A. Jamal, J.I. Lee, Reduction of CO2 emission for solar power backup by direct integration of oxy-combustion supercritical CO2 power cycle with concentrated solar power, Energy Convers. Manage. 201 (2019) 112161, https://doi.org/10.1016/j.enconman.2019.112161.
[16] A.-M. Cormos, S. Dragan, C.-C. Cormos, Integration of membrane technology for decarbonization of gasification power plants: a techno-economic and environmental investigation, Appl. Therm. Eng. 205 (2022) 118078, https://doi.org/10.1016/j.applthermaleng.2022.118078.
[17] S. Yadav, S.S. Mondal, A review on the progress and prospects of oxy-fuel carbon capture and sequestration (CCS) technology, Fuel 308 (2022) 122057, https://doi.org/10.1016/j.fuel.2021.122057.
[18] H.M. Kvamsdal, K. Jordal, O. Bolland, A quantitative comparison of gas turbine cycles with CO2 capture, Energy 32 (1) (2007) 10–24.
[19] J. Alcalde, S. Flude, M. Wilkinson, G. Johnson, K. Edlmann, C.E. Bond, V. Scott, S. M.V. Gilfillan, X. Ogaya, R. Stuart Haszeldine, Estimating geological CO2 storage security to deliver on climate mitigation, Nat. Commun. 9 (2018), https://doi.org/10.1038/s41467-018-04423-1.
[20] M. Bui, C.S. Adjiman, A. Bardow, E.J. Anthony, A. Boston, S. Brown, P.S. Fennell, S. Fuss, A. Galindo, L.A. Hackett, J.P. Hallett, H.J. Herzog, G. Jackson, J. Kemper, S. Krevor, G.C. Maitland, M. Matuszewski, I.S. Metcalfe, C. Petit, G. Puxty, J. Reimer, D.M. Reiner, E.S. Rubin, S.A. Scott, N. Shah, B. Smit, J.P.M. Trusler, P. Webley, J. Wilcox, N. Mac Dowell, Carbon capture and storage (CCS): The way forward, Energy Environ. Sci. 11 (5) (2018) 1062–1176.
[21] L.d.O. Arinelli, G.V. Brigagão, I.L. Wiesberg, A.M. Teixeira, J.L. de Medeiros, O.d. Q.F. Araújo, Carbon-dioxide-to-methanol intensification with supersonic separators: Extra-carbonated natural gas purification via carbon capture and utilization, Renew. Sustain. Energy Rev. 161 (2022) 112424.
[22] M. Branco-Vieira, M.P.C. Lopes, N. Caetano, Algae-based bioenergy production aligns with the Paris agreement goals as a carbon mitigation technology, Energy Rep. 8 (2022) 482–488.
[23] J.A. Onrubia-Calvo, A. Bermejo-López, S. Pérez-Vázquez, B. Pereda-Ayo, J. A. González-Marcos, J.R. González-Velasco, Applicability of LaNiO3-derived catalysts as dual function materials for CO2 capture and in-situ conversion to methane, Fuel 320 (2022) 123842, https://doi.org/10.1016/j.fuel.2022.123842.
[24] F. Mantei, R.E. Ali, C. Baensch, S. Voelker, P. Haltenort, J. Burger, R.-U. Dietrich, N.V.D. Assen, A. Schaadt, J. Sauer, O. Salem, Techno-economic assessment and carbon footprint of processes for the large-scale production of oxymethylene dimethyl ethers from carbon dioxide and hydrogen, Sustainable Energy Fuels 6 (3) (2022) 528–549.
[25] L. Guerra, J. Gomes, J. Puna, J. Rodrigues, Preliminary study of synthesis gas production from water electrolysis, using the ELECTROFUEL® concept, Energy 89 (2015) 1050–1056.
[26] J.F. González Álvarez, J. Gonzalo de Grado, Study of combustion in CO2-Capturing semi-closed Brayton cycle conditions, Energy 166 (2019) 1276–1290.
[27] J.F. González Álvarez, E. Alonso Fernández, Oxy-combustion flow field study under power-generating and CO2-capturing Matiant cycle conditions and its influence on the turbine inlet conditions, Fuel 303 (2021) 121172, https://doi.org/10.1016/j.fuel.2021.121172.
[28] W.A. Al-Ammari, A.K. Sleiti, Comprehensive thermoeconomic, exergoeconomic, and optimization analyses of direct oxy-combustion supercritical CO2 intercooled and reheated cycles under design and off-design conditions, Energy Sci. Eng. 10 (4) (2022) 1272–1295.
[29] A.K. Sleiti, W.A. Al-Ammari, L. Vesely, J.S. Kapat, Thermoeconomic and optimization analyses of direct oxy-combustion supercritical carbon dioxide power cycles with dry and wet cooling, Energy Convers. Manage. 245 (2021) 114607, https://doi.org/10.1016/j.enconman.2021.114607.
[30] J.F. González Álvarez, J. Gonzalo de Grado, Study of a modern industrial low pressure turbine for electricity production employed in oxy-combustion cycles with CO2 capture purposes, Energy 107 (2016) 734–747.
[31] R. Prieler, B. Mayr, M. Demuth, D. Spoljaric, C. Hochenauer, Application of the steady flamelet model on a lab-scale and an industrial furnace for different oxygen concentrations, Energy 91 (2015) 451–464.
[32] B. Mayr, R. Prieler, M. Demuth, C. Hochenauer, Modelling of high temperature furnaces under air-fuel and oxygen enriched conditions, Appl. Therm. Eng. 136 (2018) 492–503.
[33] M. Ilbas, O. Kumuk, S. Karyeyen, Numerical study of a swirl gas turbine combustor for turbulent air and oxy-combustion of ammonia/kerosene fuels, Fuel 304 (2021) 121359, https://doi.org/10.1016/j.fuel.2021.121359.
[34] M. Mehrpooya, S.A. Mousavi, M. Asadnia, A. Zaitsev, R. Sanavbarov, Conceptual design and evaluation of an innovative hydrogen purification process applying diffusion-absorption refrigeration cycle (Exergoeconomic and exergy analyses), J. Cleaner Prod. 316 (2021) 128271, https://doi.org/10.1016/j.jclepro.2021.128271.
[35] M. Mehrpooya, H. Ansarinasab, S.A. Mousavi, Life cycle assessment and exergoeconomic analysis of the multi-generation system based on fuel cell for methanol, power, and heat production, Renewable Energy 172 (2021) 1314–1332.
[36] F. Climent Barba, G. Martínez-Denegri Sánchez, B. Soler Seguí, H. Gohari Darabkhani, E.J. Anthony, A technical evaluation, performance analysis and risk

assessment of multiple novel oxy-turbine power cycles with complete CO2 capture, J. Cleaner Prod. 133 (2016) 971–985.
[37] M.H. Jahangir, R. Mokhtari, S.A. Mousavi, Performance evaluation and financial analysis of applying hybrid renewable systems in cooling unit of data centers – a case study, Sustainable Energy Technol. Assess. 46 (2021), 101220, https://doi.org/10.1016/j.seta.2021.101220.
[38] N. Khallaghi, H. Jeswani, D.P. Hanak, V. Manovic, Techno-economic-environmental assessment of biomass oxy-gasification staged oxy-combustion for negative emission combined heat and power, Appl. Therm. Eng. 196 (2021) 117254, https://doi.org/10.1016/j.applthermaleng.2021.117254.
[39] X. Wei, V. Manovic, D.P. Hanak, Techno-economic assessment of coal- or biomass-fired oxy-combustion power plants with supercritical carbon dioxide cycle, Energy Convers. Manage. 221 (2020) 113143, https://doi.org/10.1016/j.enconman.2020.113143.
[40] A.K. Sleiti, W.A. Al-Ammari, K.M. Aboueata, Flare gas-to-power by direct intercooled oxy-combustion supercritical CO2 power cycles, Fuel 308 (2022) 121808, https://doi.org/10.1016/j.fuel.2021.121808.
[41] Y. Cao, J. Zhan, Q. Cao, F. Si, Techno-economic analysis of cascaded supercritical carbon dioxide combined cycles for exhaust heat recovery of typical gas turbines, Energy Convers. Manage. 258 (2022) 115536, https://doi.org/10.1016/j.enconman.2022.115536.
[42] C. Wu, S.-S. Wang, J. Li, Exergoeconomic analysis and optimization of a combined supercritical carbon dioxide recompression Brayton/organic flash cycle for nuclear power plants, Energy Convers. Manage. 171 (2018) 936–952.
[43] L. Heller, S. Glos, R. Buck, Techno-economic selection and initial evaluation of supercritical CO2 cycles for particle technology-based concentrating solar power plants, Renewable Energy 181 (2022) 833–842.
[44] N. Peters, Turbulent Combustion, 2000, doi: 10.1017/cbo9780511612701.
[45] G.P. Smith, D.M. Golden, M. Frenklach, N.W. Moriarty, B. Eiteneer, M. Goldenberg, T. Bowman, R.K. Hanson, S. Song, W.C. Gardiner, V. v. Lissianski, Z. Qin, GRI-Mech 3.0 Reaction Mechanism, (n.d.).
[46] J. Warnatz, U. Maas, R.W. Dibble, Physical and chemical fundamental of combustion, 2006.
[47] V.L. Zimont, A.N. Lipatnikov, A numerical model of premixed turbulent combustion of gases, Chem. Phys. Rep. 14 (1995).
[48] Non-Steady Flame Propagation, 1964.
[49] V.L. Zimont, Gas premixed combustion at high turbulence. Turbulent flame closure combustion model, Exp. Therm Fluid Sci. 21 (1-3) (2000) 179–186.
[50] J. Ewald, N. Peters, A Level Set Based Flamelet Model for the Prediction of Combustion in Spark Ignition Engines Unsteady Premixed Combustion Model, International Multidimensional Engine Modeling User's Group Meeting. (2005).
[51] J. Oh, D. Noh, Laminar burning velocity of oxy-methane flames in atmospheric condition, Energy 45 (1) (2012) 669–675.
[52] R. Borghi, D. Escudie, Assessment of a theoretical model of turbulent combustion by comparison with a simple experiment, Combust. Flame 56 (2) (1984) 149–164.
[53] D. Veynante, L. Vervisch, Turbulent combustion modeling, Prog. Energy Combust. Sci. 28 (3) (2002) 193–266.
[54] O. Colin, A. Benkenida, C. Angelberger, 3D modeling of mixing, ignition and combustion phenomena in highly stratified gasoline engines, Oil Gas Sci. Technol. 58 (1) (2003) 47–62.
[55] A. Teraji, T. Tsuda, T. Noda, M. Kubo, T. Itoh, Development of a novel flame propagation model (UCFM: Universal coherent flamelet model) for si engines and its application to knocking prediction, in: SAE Technical Papers, 2005, doi: 10.4271/2005-01-0199.
[56] R.O.S. Prasad, J.P. Gore, An evaluation of flame surface density models for turbulent premixed jet flames, Combust. Flame 116 (1-2) (1999) 1–14.
[57] S.B. Pope, PDF methods for turbulent reactive flows, Prog. Energy Combust. Sci. 11 (2) (1985) 119–192.
[58] S. McAllister, J.-Y. Chen, A.C. Fernandez-Pello, Thermodynamics of Combustion, in: 2011, doi: 10.1007/978-1-4419-7943-8_2.
[59] B. Magnussen, On the structure of turbulence and a generalized eddy dissipation concept for chemical reaction in turbulent flow, in: 1981, doi: 10.2514/6.1981-42.
[60] B.F. Magnussen, B.H. Hjertager, On mathematical modeling of turbulent combustion with special emphasis on soot formation and combustion, Symp. (Int.) Combust. 16 (1) (1977) 719–729.
[61] Ross Taylor, R. Krishna, Multicomponent mass transfer I. Theory, 1993.
[62] G.D. Raithby, E.H. Chui, A finite-wolome method for predicting a radiant heat transfer in enclosures with participating media, J. Heat Transfer 112 (1990), https://doi.org/10.1115/1.2910394.
[63] A.H. Lefebvre, D.R. Ballal, Gas Turbine Combustion,Alternative Fuels and Emissions, third ed., 2010.
[64] M.P. Boyce, Gas Turbine Engineering Handbook, 2012, doi: 10.1016/C2009-0-64242-2.
[65] A.K. Sleiti, W.A. Al-Ammari, Energy and exergy analyses of novel supercritical CO2 Brayton cycles driven by direct oxy-fuel combustor, Fuel 294 (2021), 120557, https://doi.org/10.1016/j.fuel.2021.120557.
[66] A.K. Sleiti, W. Al-Ammari, S. Ahmed, J. Kapat, Direct-fired oxy-combustion supercritical-CO2 power cycle with novel preheating configurations -thermodynamic and exergoeconomic analyses, Energy 226 (2021) 120441, https://doi.org/10.1016/j.energy.2021.120441.
[67] Y.-C. Chen, N. Peters, G.A. Schneemann, N. Wruck, U. Renz, M.S. Mansour, The detailed flame structure of highly stretched turbulent premixed methane-air flames, Combust. Flame 107 (3) (1996) 223–IN2.
[68] B. Mayr, R. Prieler, M. Demuth, C. Hochenauer, The usability and limits of the steady flamelet approach in oxy-fuel combustions, Energy 90 (2015) 1478–1489.
[69] S.-M. Jeng, G.M. Faeth, Predictions of mean scalar properties in turbulent propane diffusion flames, J. Heat Transfer 106 (4) (1984) 891–893.
[70] S. Coogan, X. Gao, A. McClung, W. Sun, Evaluation of kinetic mechanisms for direct fired supercritical oxy-combustion of natural gas, in: Proceedings of the ASME Turbo Expo, 2016, doi: 10.1115/GT2016-56658.
[71] R. Anderson, H. Brandt, H. Mueggenburg, J. Taylor, F. Viteri, A power plant concept which minimizes the cost of carbon dioxide sequestration and eliminates the emission of atmospheric pollutants, in: Greenhouse Gas Control Technologies 4, 1999, doi: 10.1016/b978-008043018-8/50010-2.
[72] International Turbomachinery, International Turbomachinery Handbook 2016, (n.d.).
[73] I.B. Celik, U. Ghia, P.J. Roache, C.J. Freitas, H. Coleman, P.E. Raad, Procedure for estimation and reporting of uncertainty due to discretization in CFD applications, J. Fluids Eng. Trans. ASME 130 (2008), https://doi.org/10.1115/1.2960953.
[74] D.G. Holmes, S.D. Connell, Solution of the 2D Navier-Stokes equations on unstructured adaptive grids, in: 9th Computational Fluid Dynamics Conference, 1989, 1989, doi: 10.2514/6.1989-1932.
[75] R. Rausch, H. Yang, J. Batina, Spatial adaption procedures on unstructured meshes for accurate unsteady aerodynamic flow computation, in: 1991, doi: 10.2514/6.1991-1106.
[76] H.K. Versteeg, W. Malalasekera, An Introduction to Computational Fluid Dynamics Second Edition, in: Fluid Mechanics, 2007.
[77] J.C. Bailey, J. Intile, T.F. Fric, A.K. Tolpadi, N.V. Nirmalan, R.S. Bunker, Experimental and numerical study of heat transfer in a gas turbine combustor liner, J. Eng. Gas Turbines Power 125 (4) (2003) 994–1002.
[78] A.R. Smith, J. Klosek, A review of air separation technologies and their integration with energy conversion processes, Fuel Process. Technol. 70 (2) (2001) 115–134.
[79] P.N. Dyer, R.E. Richards, S.L. Russek, D.M. Taylor, Ion transport membrane technology for oxygen separation and syngas production, Solid State Ionics 134 (2000), https://doi.org/10.1016/S0167-2738(00)00710-4.
[80] J. Oh, Spectral characteristics of a premixed oxy-methane flame in atmospheric conditions, Energy 116 (2016) 986–997.
[81] Y.-H. Li, G.-B. Chen, Y.-C. Lin, Y.-C. Chao, Effects of flue gas recirculation on the premixed oxy-methane flames in atmospheric condition, Energy 89 (2015) 845–857.
[82] T. Best, K.N. Finney, D.B. Ingham, M. Pourkashanian, Impact of CO2-enriched combustion air on micro-gas turbine performance for carbon capture, Energy 115 (2016) 1138–1147.
[83] D. Novales, A. Erkoreka, V. De la Peña, B. Herrazti, Sensitivity analysis of supercritical CO2 power cycle energy and exergy efficiencies regarding cycle component efficiencies for concentrating solar power, Energy Convers. Manage. 182 (2019) 430–450.